AD_____

Award Number: W81XWH-04-2-0022

TITLE: Development of a Multileaf Collimator for Proton Radiotherapy

PRINCIPAL INVESTIGATOR:　　　　　James McDonough, PhD

CONTRACTING ORGANIZATION:　University of Pennsylvania,
　　　　　　　　　　　　　　　　　Philadelphia PA 19104-6205

REPORT DATE: June 2010

TYPE OF REPORT: Annual

PREPARED FOR:　　U.S. Army Medical Research and Materiel Command
　　　　　　　　　Fort Detrick, Maryland 21702-5012

DISTRIBUTION STATEMENT:

　⊠ Approved for public release; distribution unlimited

The views, opinions and/or findings contained in this report are those of the author(s) and should not be construed as an official Department of the Army position, policy or decision unless so designated by other documentation.

REPORT DOCUMENTATION PAGE			*Form Approved* OMB No. 0704-0188

Public reporting burden for this collection of information is estimated to average 1 hour per response, including the time for reviewing instructions, searching existing data sources, gathering and maintaining the data needed, and completing and reviewing this collection of information. Send comments regarding this burden estimate or any other aspect of this collection of information, including suggestions for reducing this burden to Department of Defense, Washington Headquarters Services, Directorate for Information Operations and Reports (0704-0188), 1215 Jefferson Davis Highway, Suite 1204, Arlington, VA 22202-4302. Respondents should be aware that notwithstanding any other provision of law, no person shall be subject to any penalty for failing to comply with a collection of information if it does not display a currently valid OMB control number. **PLEASE DO NOT RETURN YOUR FORM TO THE ABOVE ADDRESS.**

1. REPORT DATE *(DD-MM-YYYY)*	2. REPORT TYPE	3. DATES COVERED *(From - To)*
01-06-2010	Annual	17 May 2009 – 16 May 2010

4. TITLE AND SUBTITLE	5a. CONTRACT NUMBER
Development of a Multileaf Collimator for Proton Radiotherapy	
	5b. GRANT NUMBER
	W81XWH-04-2-0022

6. AUTHOR(S)	5d. PROJECT NUMBER
Chris Ainsley PhD, Steven Avery PhD, Derek Dolney PhD, James Durgin, Richard Maughan PhD, James McDonough PhD, James Metz MD, Zelig Tochner MD, Arnaud Belard, Yu Chen PhD, Rulon Mayer PhD, LTC John O'Connell MD	
	5e. TASK NUMBER
	5f. WORK UNIT NUMBER

7. PERFORMING ORGANIZATION NAME(S) AND ADDRESS(ES)	8. PERFORMING ORGANIZATION REPORT NUMBER
University of Pennsylvania Philadelphia PA 19104-6205	

9. SPONSORING / MONITORING AGENCY NAME(S) AND ADDRESS(ES)	10. SPONSOR/MONITOR'S ACRONYM(S)
U.S. Army Medical Research and Materiel Command Fort Detrick, Maryland 21702-5012	
	11. SPONSOR/MONITOR'S REPORT NUMBER(S)

12. DISTRIBUTION / AVAILABILITY STATEMENT

Approved for public release; distribution unlimited

13. SUPPLEMENTARY NOTES

14. ABSTRACT
This report describes the sixth year of a project to design and construct multileaf collimators (MLC) to be used in proton radiotherapy, the fifth year of the project to develop scanned beam technology for proton radiotherapy, and the fourth year of the project to develop image guided treatment protocols for proton therapy. This research project is a joint collaborative effort between the University of Pennsylvania (HUP) and the Walter Reed Army Medical Center (WRAMC) and is part of a larger project to build a state-of-the-art proton radiotherapy facility in Philadelphia.
The accomplishments during the past year of the project are described in this report.

15. SUBJECT TERMS
Radiation Oncology, Proton Therapy, Multileaf Collimator, MLC, Conformal Radiotherapy

16. SECURITY CLASSIFICATION OF:			17. LIMITATION OF ABSTRACT	18. NUMBER OF PAGES	19a. NAME OF RESPONSIBLE PERSON USAMRMC
a. REPORT	b. ABSTRACT	c. THIS PAGE	UU	57	19b. TELEPHONE NUMBER *(include area code)*
U	U	U			

Standard Form 298 (Rev. 8-98)
Prescribed by ANSI Std. Z39.18

Table of Contents

Introduction

The overall goal of this multi-year research project in collaboration with the Walter Reed Army Medical Center is to develop the necessary technology to make the proton facility that is being constructed in Philadelphia the most advanced proton radiotherapy center. The first technology is the development of a multileaf collimator (MLC) for proton therapy and investigates the issues that must be resolved to use an MLC in proton therapy. The second technology under study is the optimization of the spot-scanning delivery technique including the effects of organ motion. The third technology is the development of protocols to apply the techniques of image-guided and adaptive radiotherapy to proton therapy, and to develop a decision-making algorithm to maximize the efficiency of the facility. This report describes the progress during the sixth year of the expected seven year process. Included in that progress are the following activities and achievements: (1) Use of the GEANT4 Monte Carlo code, which was developed in the previous years of the project, to test various MLC designs culminating in the delivery of the first MLC and the status of the on-going tests of that MLC; (2) Use of the same simulation program to optimize the dose distribution from scanned beams accounting for inhomogeneities and organ motion; (3) The developing treatment protocols and understanding the factors that are involved to efficiently utilize the beam; and (4) Advance the interconnectivity between the department at Penn and the Walter Reed Army Medical Center to permit remote treatment planning.

Body

In June 2006, following years of defining specifications and evaluating proposals, the University of Pennsylvania Health System (UPHS) signed a contract with Ion Beam Applications, S.A. (IBA). In addition to the details associated with the delivery of a proton therapy system the contract included three development agreements directly related to the work supported by this grant to develop technology for proton therapy. The development agreements between UPHS, IBA and Varian Medical Systems, Inc. (the leading conventional radiotherapy vendor) were: (1) to develop a multileaf collimator for the IBA proton delivery system, (2) to develop a cone-beam CT to permit imaging of the patient in the treatment room, and (3) to develop the pencil-beam scanning algorithm of the Varian treatment planning system.

Much of the effort in the past year has been to: (1) install and commission the final MLC for clinical use; (2) design a system that permits the treatment of shallow targets with scanned beams; and (3) write treatment protocols and submit them to regulatory bodies for approval. The MLC project is essentially complete, which has the highest priority because the treatment rooms cannot be commissioned without it, is the most advanced of these projects. The scanning development continues but the clinical implementation has been delayed by approximately one year because we did not feel that the IBA system was mature enough for routine clinical use. The cone-beam CT development has made the least progress thus far but we continue to work with several vendors and other proton facilities to find an affordable solution. It has only recently been introduced to conventional radiotherapy and is constantly being upgraded. Our challenge is to design a device that will be able to easily follow the advances the system makes in conventional therapy.

This report concentrates on the sixth year achievements of the multileaf collimator development, the fifth year of work on the spot-scanning/motion project, and the fourth year on the development of image-guided and adaptive radiotherapy protocols. The Statement of Work in the approved grant proposals included the following items to be investigated. (Note: to minimize confusion, the years in which we expected to perform the work have been replaced by the fiscal year because there are three separate starting dates.) Because of the delay in choosing the vendor several of the aims that were originally planned to be completed by now are still ongoing. The items in the Statement of Work are listed below with a comment on the status of any item that was to have work performed by this time.

MLC Development

1. Leaf design: (FY 2005). This is complete.

2. Joint Military/Civilian Proton Radiotherapy Center: (FY 2005-2006). The first stage of this was completed in 2007. A more complete system, which satisfies DOD patient confidentiality, is discussed in Section IV of this report.

3. Investigate the design factors affecting the lateral penumbra of the beam: (FY 2005). Section I describes our current investigation of this.

4. Design of the MLC system: (FY 2005). This is complete except for the write-up and publication.

5. Production of a prototype MLC and initial testing: (FY 2006). The prototype was tested at the Jacksonville proton facility in September 2008.

6. Incorporation of the MLC design into the treatment planning system: (FY 2006). This work is complete although we still have some suggested improvements that Varian may include in their product.

7. Production of MLCs for gantry and fixed-beam rooms: (FY 2007-2009). The first MLC arrived in February 2009 and the fourth, and final, was delivered in March 2010.

8. Commissioning MLCs for gantry and fixed-beam rooms: (FY 2007-2009). Two MLCs have been commissioned. In the current schedule the third will be done in September 2010 and the fourth in March 2011.

9. Adapt the system to include collimation on a layer-by-layer basis: (FY 2007-2009). This is an area where there has not been much progress.

Spot-Scanning development

1. Scan optimization: (FY 2006). This work began in 2006 and is continuing. The current status is detailed in Section II.

2. Patient motion simulation: (FY 2006-2007). We are able to perform simulations of 4D CT sets, but as discussed in Section II we need to increase the memory to deal with the large number of CT slices.

3. Development of phantom for motion studies: (FY 2007-2008). We decided to purchase a phantom for motion studies rather than building one ourselves.

4. Development of dosimetry systems for scanned beams: (FY 2006-2009). We are investigating dosimetry systems for use with scanned beams and will either purchase a system when one becomes available or work with the physics department to develop one.

5. Production of beam scanning nozzle and initial testing: (FY 2008-2010). During the past year the first patient treatment at an IBA proton facility occurred at Massachusetts General Hospital. Because of the significant challenges that still exist we will not accept a room with that technology until late 2010.

6. Incorporation of beam scanning in the treatment planning: (FY 2007-2010). We continue to use the Monte Carlo generated "beam data" with Varian's scanning algorithm in the Eclipse treatment planning system. This gives us the ability to evaluate patient plans from scanned beams prior to commissioning the system.

7. Commissioning of beam scanning nozzle for gantry rooms: (FY 2008-2010). This is delayed until early 2011.

8. Measurement of dose distributions in static and moving phantoms: (FY 2008-2010). This is delayed until early 2011.

9. Joint Military/Civilian Proton Therapy Center telemedicine system: (FY 2006-2007). As described in Section IV, and in earlier reports, we have struggled to find a secure DOIM-approved solution that permits multipoint conferencing with shared applications over the internet.

Image-guided and adaptive radiotherapy development

1. Pre-treatment Imaging for Volume Definition: (FY 2008-2009). Several imaging protocols are approved at Penn. However it has been determined that they will not be reviewed by TATRC because no funds will be used to run the studies. The protocols that WRAMC plan to participate in will be reviewed by DOD.

2. Pre-treatment Imaging for Monitoring and Quantifying Tumor and Normal Tissue Motion: (FY 2008-2009). A protocol to study this was approved by the Penn IRB and is currently being reviewed by Dr Jeffery Stephenson at TATRC.

3. Pre-treatment Patient Set-up Using Cone-Beam CT and Other On-Board Imaging Techniques: (FY 2009-2011). The set-up room is being used for patient setups prior to proton therapy as of January 2010.

4. Cone Beam CT on the Gantry: Imaging at the Time of Treatment: (FY 2009-2011). We are still searching for a vendor that can provide an affordable CT system for proton rooms. This is discussed in Section III.

5. Re-imaging/replanning During the Course of Treatment: (FY 2008-2011). A protocol to study this was approved by the Penn IRB and is currently being reviewed by Dr Jeffery Stephenson at TATRC. It is the same protocol in #2.

6. Development of Imaging Protocols: (FY 2007-2008). This work is on-going though, as discussed in Section III, it is no longer considered part of the SOW.

7. Development of an efficient schedule system: (FY 2007-2008). This work showed great promise and was expanded as part of phase 5 of this project and will be reported in the reports for W81XWH-07-2-0121.

Progress

The work over the last year can be broken into three areas relating to: (I) MLC development, (II) spot-scanning development, (III) protocol development, and (IV) work at Walter Reed as a subcontractor and collaborator.

I.   MLC progress

Now that two rooms have been commissioned for treatment using double scattering mode and we have data with which to verify our Monte Carlo model, we have begun preparing our simulation model for individual treatment plan verification. We have also continued to investigate the differences between calculated dose distributions from

Eclipse and dose distributions that have been measured, as was described in the April 2010 quarterly report. To do so we have been examining the distribution of dose deposited by protons scattered from within the MLC leaves, which we have proposed to be at least partially responsible for the Eclipse-measurement differences.

To validate our simulation model, we made comparisons between measurements taken during commissioning of the first treatment room and Monte Carlo simulations for the same treatment parameters. The results of the comparisons can be found in the January 2010 quarterly report. While the comparisons generally match well, there is still room for improvement with the simulation. We have been working on optimizing the kinetic energy spread of the beam and re-optimizing the beam current modulation files based on the measurements that are now available from our beams. More recently, we have been comparing small field data measured in a water tank with simulations for the same small fields.

In order to successfully model individual treatment plans in our simulation, we needed to create a phantom that could be composed of multiple materials based on the components of a patient's body read from a CT scan. This was accomplished using G4PhantomParameterisation which allows each user-defined voxel of the phantom to be composed of a different material. After creating the parameterized phantom, we used it to look into a possible issue with the way Eclipse calculates dose deposition in materials other than water. For patient treatment verification, in addition to a patient-specific phantom, the simulation also requires the ability to read in and use MLC leaf positions from Eclipse treatment plans and to be able to construct patient-specific range compensators based on the DICOM file that is sent from Eclipse to the milling machine to build the physical compensator. Through these studies, we are bringing the simulation model closer to being able to be used as a second check for treatment planning calculations.
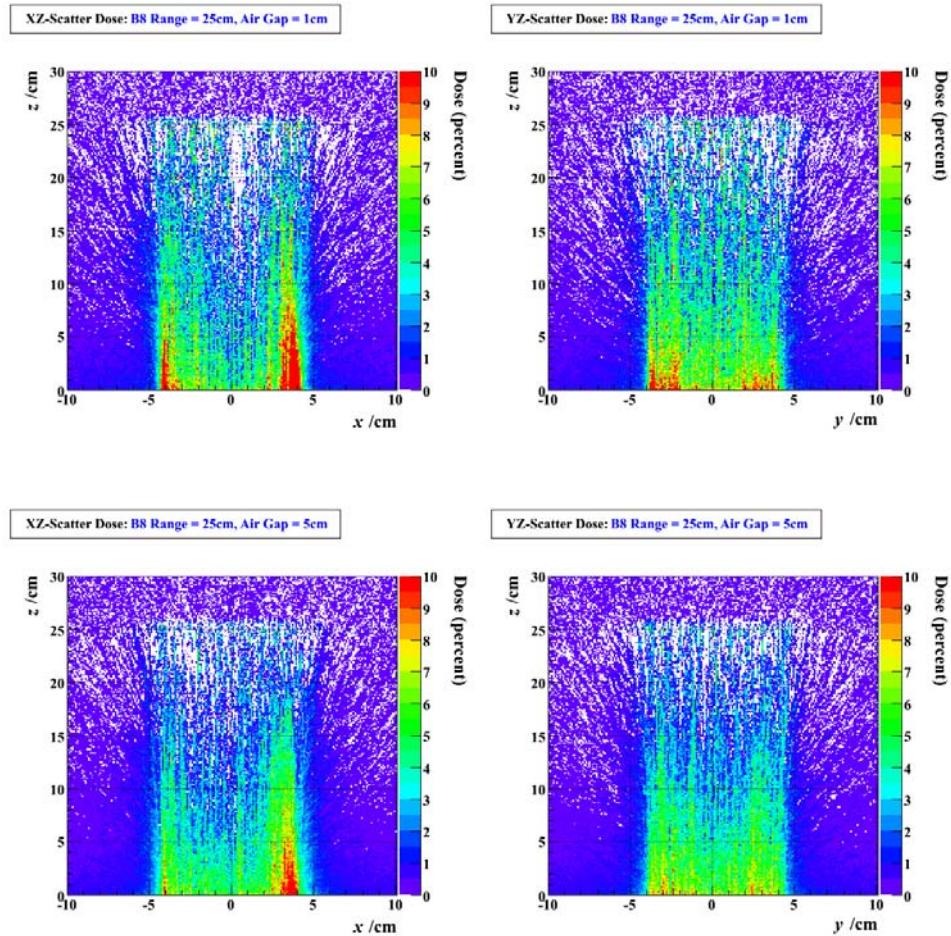

Scatter contributions as a function of MLC-to-phantom air gap

We began investigating differences between measurements in a water tank and dose distributions calculated in Eclipse in our previous report. The SOBPs calculated in Eclipse differed most from those measured during commissioning for higher energy options near the entrance to the water phantom. We speculated that the differences between Eclipse calculation and measurement were due, at least in part, to the absence in block scattering from the Eclipse model. For this reason, we were interested in the dose contribution from protons that scatter into the field from within the MLC leaves. We looked at the contribution of edge scatter to SOBP dose curves by running pairs of simulations, one with and one without edge scattered protons, for the same beamline settings.

To further study the dose due to scatter from within the MLC leaves, we created 2-dimensional profiles of the dose resulting from edge scattered protons as a function of MLC-to-phantom air gap. Since the effect of dose from leaf-scattered protons increases with increasing energy option, we looked at scattered dose for double scattering option B8 with a range of 25 cm with a 10 cm modulation. 2D scattered dose distributions were created by running a pair of simulations at each air gap of 1, 5, 8, 10, and 15 cm with the same beamline settings, killing the leaf-scattered protons in one simulation of each pair. Killing the protons that enter the MLC leaves excludes the dose due to edge-scattered protons. The dose distribution excluding protons entering the MLC leaves was then subtracted from the dose distribution including dose from all protons so that the dose remaining could be attributed to the edge-scattered protons. We also figured out that the same plots can be generated with a single simulation by tagging protons (and their daughter particles) that have stepped into the MLC leaves, and only counting dose deposited by the tagged particles.

Figure 1 contains the 2D distributions of dose from edge scattered protons projected in the X-Z and Y-Z planes as a function of air gap for a 10x10 cm^2 field size. The dose is integrated through the y-direction for the X-Z projection and through the x-direction for the Y-Z projection and normalized to the dose in the middle of the SOBP and multiplied by 100 to show the percentage of dose contributed by edge scatter. As we have seen before, there is a higher dose contribution from edge scattered protons at the edge of the field in the direction of leaf travel (x-direction) at the entrance to the water phantom, which can be seen in the X-Z projections. The horns from the edge scattered protons at an air gap of 1cm on entrance to the water phantom constituted up to 12 percent of the total dose in the middle of the SOBP. Also the horn at +x is larger than that at -x due to the asymmetry in the leaf ends of opposing banks. The Y-Z projections show that dose from edge-scattered protons is distributed more evenly across the y-direction which is perpendicular to the direction of leaf travel. The dose from edge scattered protons decreases

overall with increasing air gap, and the distinction of the horns in the direction of leaf travel also decreases with air gap. At larger air gaps, the dose due to edge scattered protons at shallow depths in the water phantom is shown to be around 5-7% of the mid-SOBP dose. This is on the order of the difference between measured SOBPs and those calculated in Eclipse near the entrance of the water phantom for higher energy options which were shown in the April 2010 quarterly report. These results support the idea that dose from protons scattering back into the field from within the MLC leaves is likely a source of difference between measured dose distribution and those calculated by Eclipse.
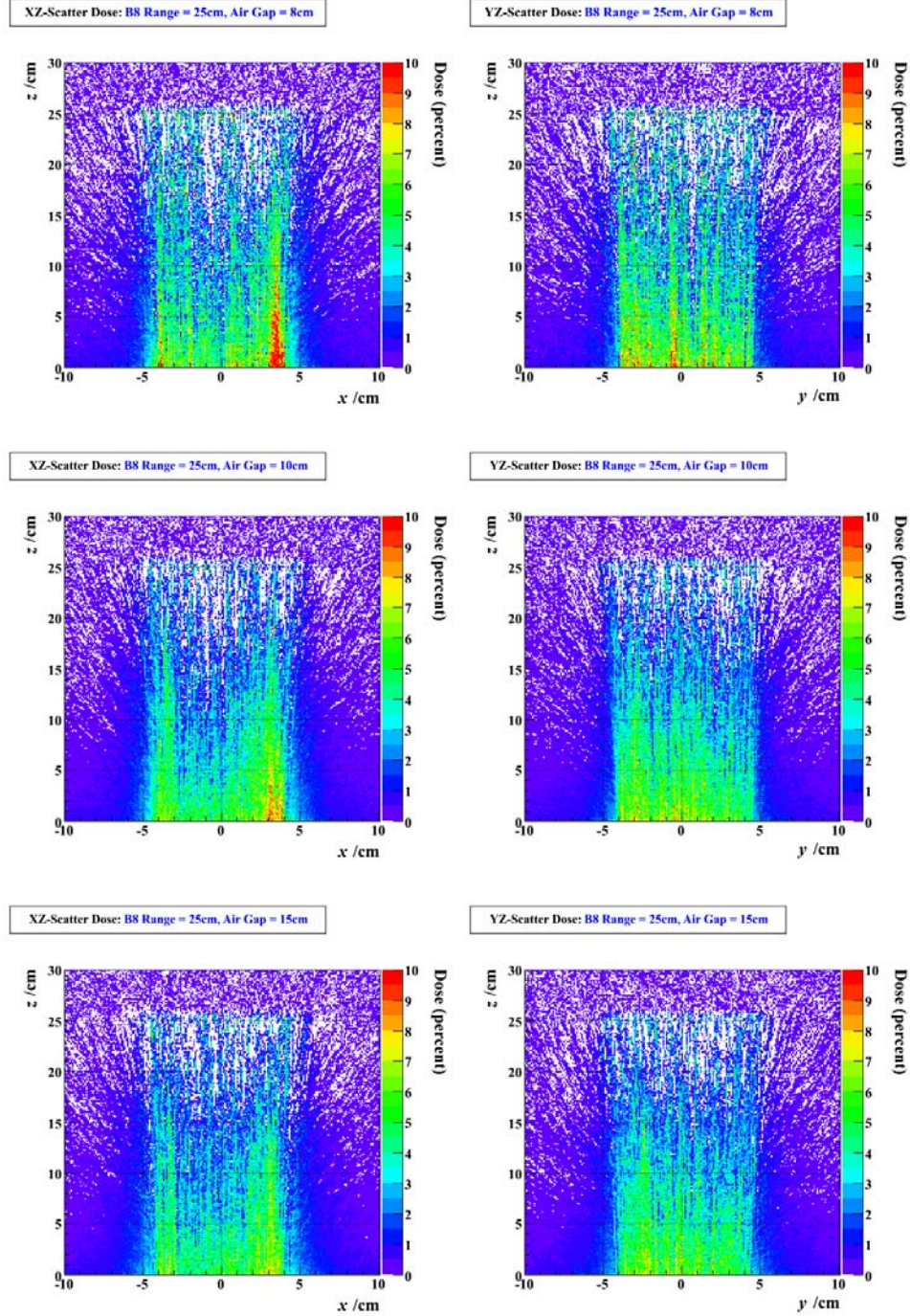
Figure 1: 2-Dimensional distributions of dose due to edge scattered protons as a function of air gap for double scattering option B8 with a range of 25 cm and a modulation of 10 cm. Simulations were run at MLC-to-phantom air gaps of 1, 5, 8, 10, and 15cm for a 10x10cm² field size. The two dimensional dose projections were normalized to the dose in the center of the SOBP of the simulation including dose from edge scatter, and the scatter dose is shown as a percent. The XZ-projections which have been integrated through the y-direction are shown on the left and the YZ-projections which have been integrated through the x-direction are shown on the right. The XZ-projections include the direction of leaf travel and show an elevation of dose due to scatter at the field edge on entrance to the water phantom consistent with the "horns" that have been seen in the past. The contribution of dose from edge scattered protons decreases with increasing air gap and the

9

elevated dose at the field edge in the direction of leaf travel also decreases with increasing air gap.

Small field simulation verification

For the verification of our simulation model, we have compared data from measurements taken during commissioning with simulations using the same beamline parameters. The results of these comparisons can be found in the January 2010 quarterly report. All of the comparisons between our simulation model and measurements up to this point have been for field sizes 5x5 cm^2 or larger. Since we want our simulation to be as accurate as possible with respect to measurements from our proton facility, we have begun verifying Monte Carlo results for small fields with measurements. We ran simulations corresponding to measurements that have been run for small circular field sizes.

Measurements of pristine peaks with a range of 24.67 cm (double scattering option B8) were taken using a circular MLC shape with diameters of 15, 10, 7.5, 5, 3, 1.8, and 1 cm at an elevation of 25 cm with an MLC-to-phantom air gap of 15 cm. Simulations were run using the same geometry into a 40x40x40 cm^3 water tank, and the data from measurement and simulation are plotted in Figure 2. The Monte Carlo data have been integrated over a 1x1 cm^2 area and the histograms have been normalized so that the maximum of the peak of the 15 cm diameter field size simulation data matches with the maximum of the 15 cm diameter field size measurement data. The simulation data matches well with the measured small field data and shows that there is no noticeable difference in the dose distribution for circular fields with diameters greater than 5 cm. The maximum dose of the pristine peak begins to decrease for the circular field with a 3 cm diameter, and for field sizes with diameters less than 3 cm, the entrance dose as well as the peak dose decreases with decreasing field size.

In addition to pristine peaks, SOBPs with a range of 17.5 cm and modulation 10 cm (double scattering option B6), were measured and calculated in Eclipse for circular fields with diamaters of 1.8, 3, and 10 cm. Simulations were run with the same treatment parameters for circular fields with diameters of 1, 1.8, 3, and 5cm. For small field sizes, the shape of the depth dose curves from the simulation is highly dependent on the area over which the dose is integrated through the center of the water phantom. Figure 3 contains comparisons of the measurement, Eclipse, and simulation SOBPs as a function of the area used to integrate dose in the simulation. Measurements match the simulation closely for integration areas around 1.2x1.2cm^2 and 1x1cm^2, but the simulation deviates from the measurement data when larger or smaller areas of integration are used. Presumably, this is the effective collecting area of the PPC05 chamber (~0.8 cm^2). The SOBP calculated in Eclipse does not show as large of a drop in central axis dose for a circular field with a 1.8 cm diameter as the measurement for the same field size. The simulation begins to approach the SOBP calculated in Eclipse as the area of integration is reduced.
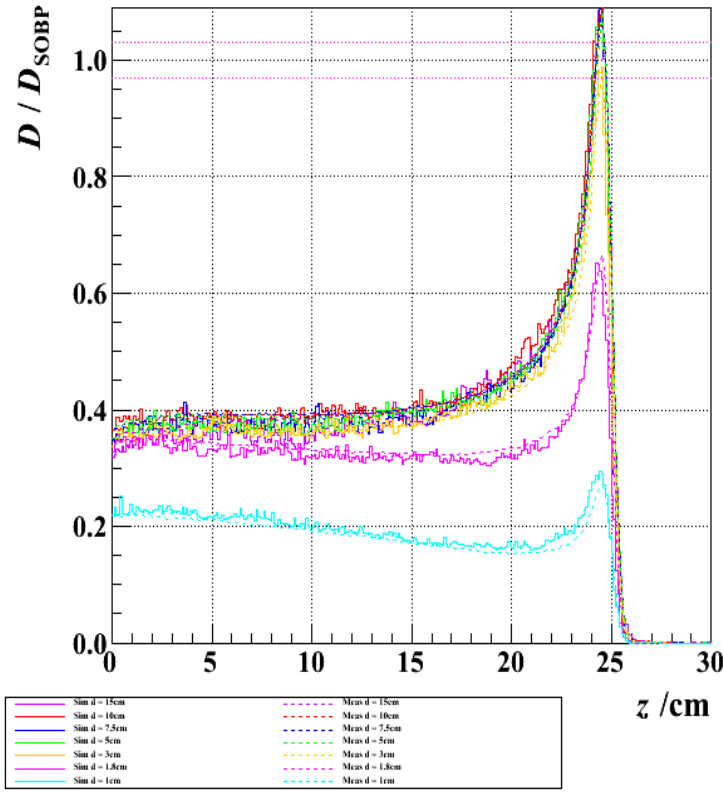
Figure 2: Pristine peaks for double scattering option B8 with range 24.67 cm for circular field sizes with diameters 15 cm (purple), 10 cm (red), 7.5 cm (blue), 5 cm (green), 3 cm (yellow), 1.8 cm (pink), and 1 cm (light blue). The solid lines are the simulation data and the dotted lines are the measurement data. The simulation data was done in a 20x20x40 cm^3 water tank and was integrated over a 1x1 cm^2 square through the center of the phantom and the measurement data was taken in a water tank with a PPC05 chamber.

B6 range = 17.5cm, modulation = 10cm, 2cm integration
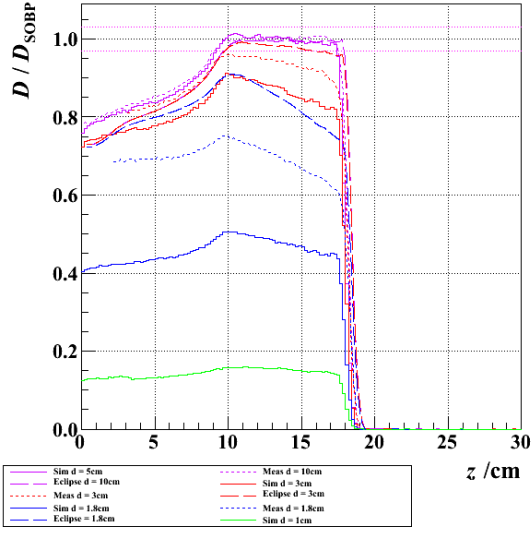
B6 range = 17.5cm, modulation = 10cm, 1.4cm integration
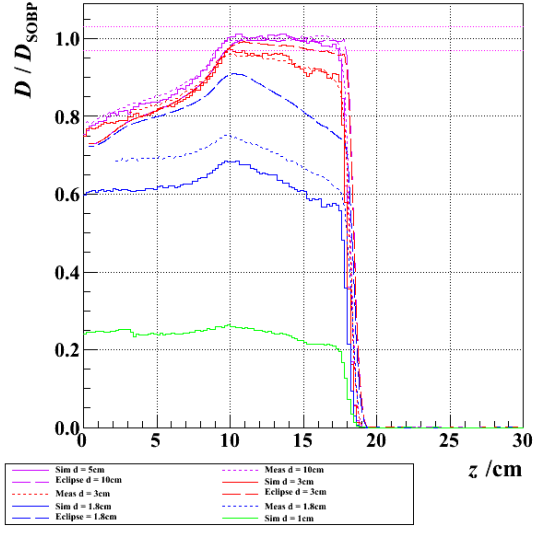
B6 range = 17.5cm, modulation = 10cm, 1.2cm integration
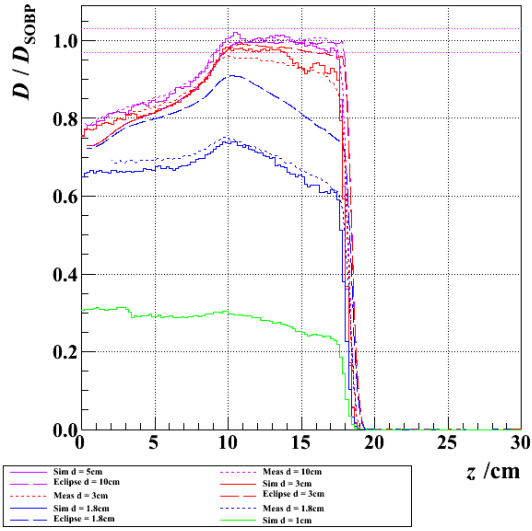
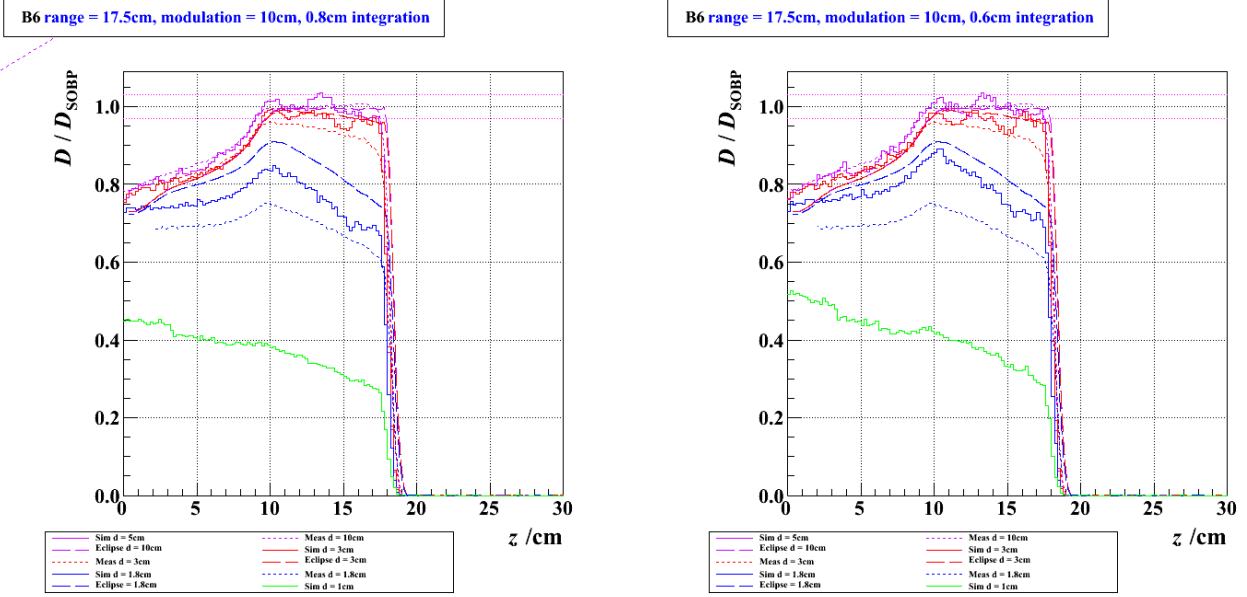**B6 range = 17.5cm, modulation = 10cm, 1cm integration**

12
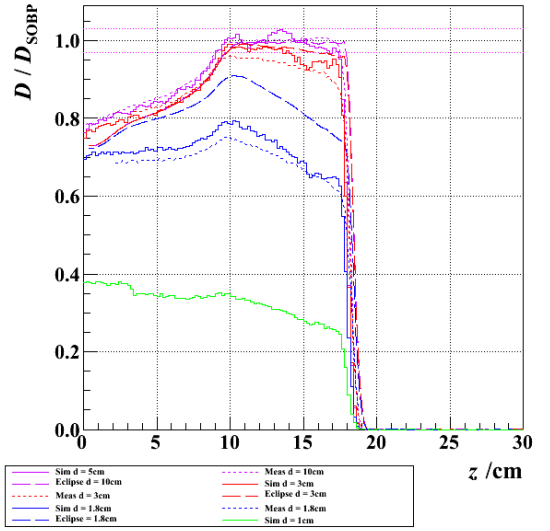
Figure 3: A comparison between SOBPs for multiple circular field sizes measured in a water tank with a PPC05 chamber, calculated in Eclipse, and simulated in a water phantom. The SOBPs have a range of 17.5 cm and a modulation of 10 cm and were measured for circular field sizes with 10, 3, and 1.8 cm diameters and simulated using circular field sizes of 5, 3, 1.8, and 1 cm diameters. There is no noticeable difference for field sizes with diameters greater than 5 cm, so the simulation with 5 cm diameter field size corresponds with the measured SOBP for a 10 cm diameter field size. The SOBPs from the simulations have been obtained by integrating the dose over different areas through the center of the phantom in order to produce the depth dose curve. The square areas over which the dose was integrated are 2x2, 1.4x1.4, 1.2x1.2, 1x1, 0.8x0.8, and 0.6x0.6 cm^2.

Preparing simulation for treatment plan verification

A new parameterized phantom was created in our simulations to have the flexibility of making each voxel of the sensitive detector from a different material using the G4PhantomParameterisation class. This ability is useful for creating a phantom using 3D patient information that can be read from a CT scan. The energy deposited in each voxel of the phantom is scaled inversely by the volume and density of the material where the energy is deposited to convert the energy to dose.

To verify that the parameterized phantom was created correctly, a fully modulated beam of double scattering option B6 was run into a phantom composed completely of water and a phantom with a 2cm thick layer of lead sandwiched between two layers of water at a depth of 4 cm. The resulting SOBPs can be seen in Figure 4. The mass stopping power ratio of lead to water is approximately ½ for the proton energy used and the density ratio of water to lead is 11.35, so we expect the water equivalent thickness of the 2cm of lead to be around 11.35 cm. The lead is located at a depth of 4cm, so the range of the beam should be reduced to about 8.2 cm when the layer of lead is in place. The simulation with the composite phantom resulted in a depth dose curve that looked as expected with the predicted range and with the dose deposited in the lead reduced by approximately ½.

Once we confirmed the simulation was working using a phantom composed of multiple materials, we wanted to verify Eclipse's treatment of inhomogeneities in the proton beam. A 40x40x40cm³ phantom composed of water with 3 cm of cortical bone was created in Eclipse as well as in our simulation. A beam with a range of 25 cm and modulation of 15 cm was used and the layer of bone was located at a depth of 17.5 cm so that it would be in the center of the SOBP. The cortical bone used in the simulation has a proton stopping power of 1.71 relative to water and a density of 1.92 g/cc. Figure 5 shows a comparison of SOBPs for these treatment parameters run into a phantom made completely of water in Eclipse and in our Monte Carlo. The curves match well except for the dose near the entrance where, as was mentioned above, the difference is partially attributed to Eclipse's inability to model

13

edge scatter off of the MLC leaves. The second image of Figure 5 shows the SOBPs for Eclipse and simulation with the composite phantom of water and bone in place. The Monte Carlo shows a drop in dose in the layer of bone, consistent with its mass stopping power ratio of 1.71/1.92 = 0.89, while Eclipse calculates a slight increase in dose through the bone.

To figure out what Eclipse was doing in order to calculate inhomogeneity corrections for the dose through the layer of bone, we began to manipulate the SOBP calculated by Eclipse when run through the phantom made of only water. First we corrected the range of the protons for the SOBP in water to adjust for the water equivalent thickness of bone. This curve had the same range as the Eclipse SOBP for the composite phantom but did not show the increase in dose within the layer of bone. We then corrected the SOBP with the corrected range for the inverse square of distance since the protons were not traveling as far when passing through the bone. This adjusted SOBP matched almost exactly with the SOBP Eclipse calculates when using the composite phantom. For this reason we believe that Eclipse is making corrections for the range and inverse square of distance for the dose deposited through the bone, but is not scaling the energy deposited by the mass stopping power ratio of bone. All of the curves mentioned can be seen in the last image of Figure 5.
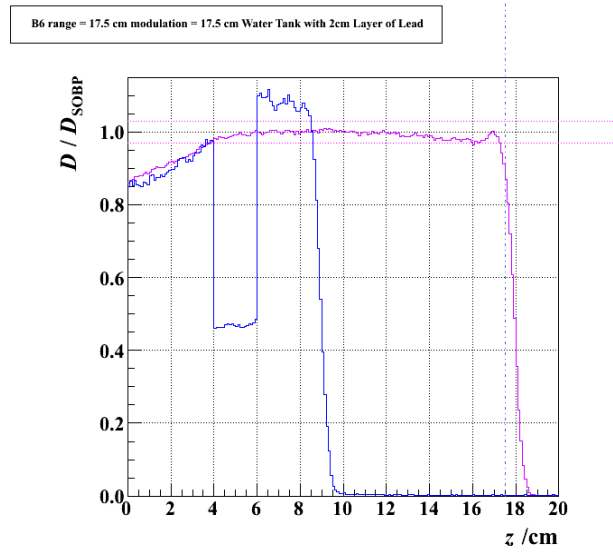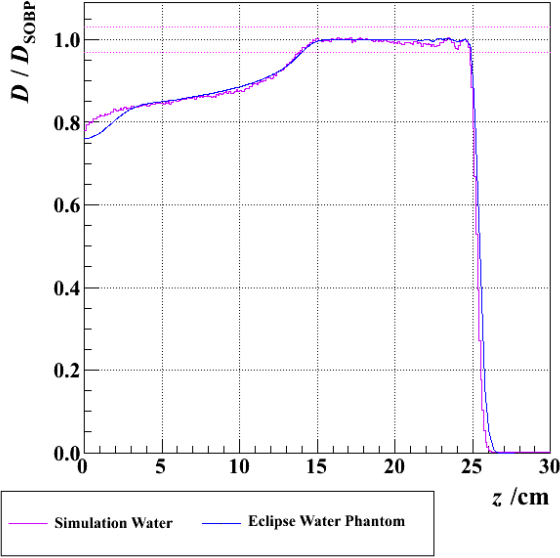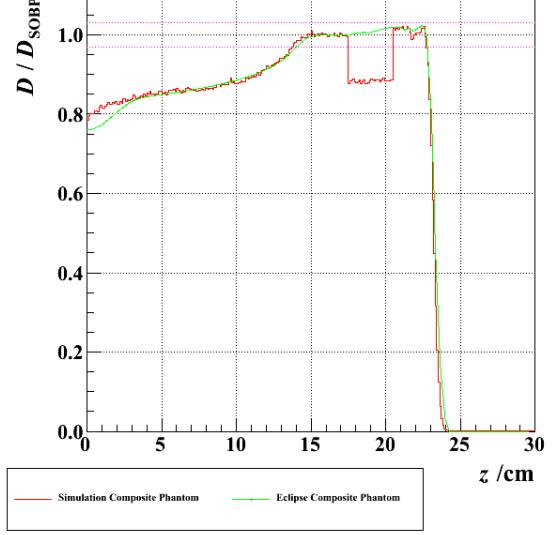

Figure 4: SOBPs simulated with a range of 17.5cm and full modulation into a phantom made of all water (purple) and a phantom made of water with a 2cm layer of lead located at a depth of 4cm (blue).
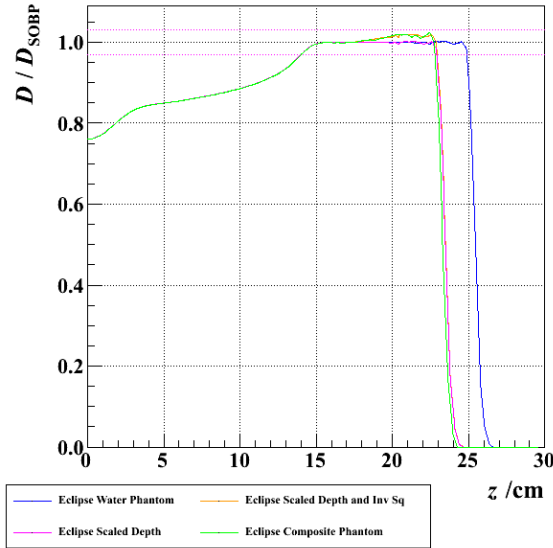
14

Figure 5: Comparison of SOBPs modeled in our simulation and calculated in Eclipse. All of the SOBPs have a water-equivalent 25 cm range and 15 cm modulation with a $10\times10\text{cm}^2$ square field size. The first pair of SOBPs (top) compare simulation (purple) and Eclipse (blue) depth dose curves run in $40\times40\times40\text{cm}^3$ water tanks. The second pair of curves (center) compares simulation (red) and Eclipse (green) depth dose curves run into a composite phantom with a 3 cm layer of cortical bone centered at a depth of 17.5 cm. The third set of curves (bottom) shows the Eclipse calculated SOBP run in the water phantom (blue), the SOBP from the water phantom with range corrected for the water equivalent thickness of the bone (red), the SOBP from the water phantom with the dose corrected for the reduced range and the inverse square of dose deposited (orange), and the SOBP calculated by Eclipse when using the composite phantom (green).

The next part of preparing the Monte Carlo for patient-specific simulation was developing the ability to extract treatment information from Eclipse to obtain MLC leaf positions and to create individual range compensators in the

15

simulation. Using the DICOM information from Eclipse we have been able read out treatment parameters and position the MLC leaves correctly. Figure 5 shows an MLC configuration in Eclipse along with a visualization of the simulation geometry and also a dose distribution from a simulation verifying correct leaf positions and coordinate system correlation.

The compensator is created by using the milling drill diameter, milling hole coordinates, and compensator thicknesses read into the simulation from a file. Subtraction volumes are then created at each milling hole coordinate with appropriate thicknesses and subtracted from a solid Plexiglas box leaving a model of the physical compensator remaining. At this point, the geometry of the compensator is too complicated for our visualization tool to recreate for verification and the simulations using the compensator take a very long time to complete, seemingly because of the complicated array of volume boundaries, created by the many Boolean operations, that Geant4 must then track particle histories through. We will continue to work on improving this process and verifying that the compensator is being created correctly.
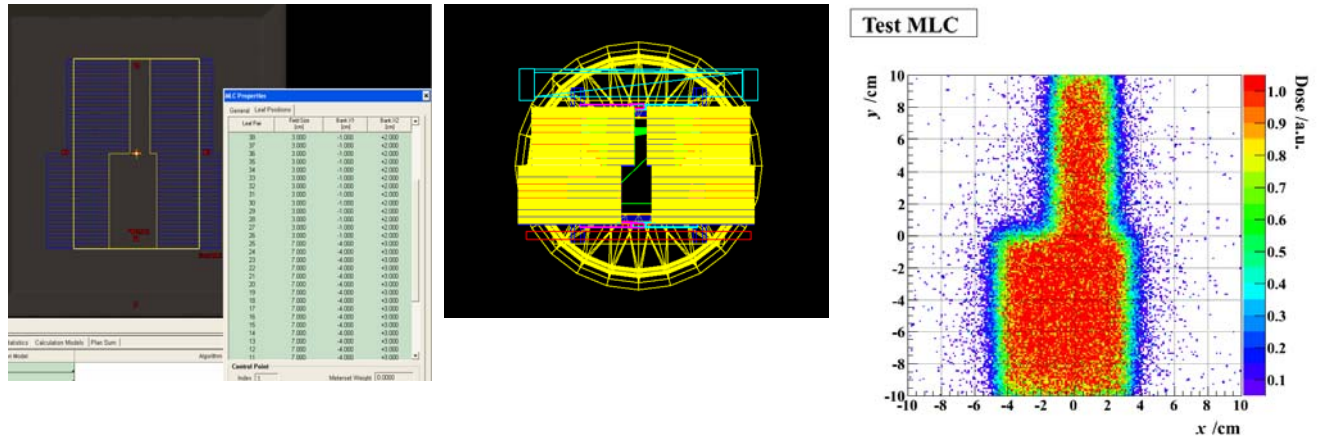

Figure 5: Verification of leaf positions being read from Eclipse into the simulation. The leaf configuration from Eclipse (left) matches with the visualization of the simulation treatment geometry (center) as well as the field of dose distribution for a simulation using the Eclipse parameters.

II.   Spot-scanning progress

Spot Optimization

Over the past year, a lot of progress has been made on the simulation code for pencil beam scanning. The spot-weight optimization code, begun by Josh Scheuermann, developed further by Mark Ingram, and these last two years improved by Derek Dolney, is where most of the spot scanning research and develop has been focused. Those developments are summarized below, followed by a description of the progress made during the last quarter. The spot weight optimization code will be used to benchmark the commercial Eclipse treatment planning system used at HUP, especially its modeling of tissue inhomogeneities, and as a tool for the optimization of beam modification devices (range shifter, ridge filter) and delivery techniques (patient-specific bolus, aperture scanning).

In addition, some new research tools have been developed. These were described in previous quarterly reports, and include extraction of treatment plan information from DICOM files (pencils beam spot positions, energies, and intensities; MLC leaf positions; and the compensator milling pattern), and the ability to perform the forward dose calculation: given a CT dataset and a scanned beam treatment plan file, we can calculate the dose distribution using accurate Monte Carlo simulations. This capability will be used to validate the Eclipse, especially for difficult cases, and as the basis for dose calculations to 4D CT datasets for future studies considering patient motion, margin sizes, and robust treatment planning.

The remainder of this section will summarize the improvements made to the spot-weight optimization code over the past year. There are significant pieces to the spot weight optimization procedure: the generation of the pencil beam kernels (one dose kernel for each pencil beam target position), and the optimization of the intensities (or "weight") of each kernel to best achieve dose objectives input by the treatment planner. The kernel generation step uses Geant4 Monte Carlo to track protons through a phantom constructed from a CT dataset of the patient using a calibration that maps the CT Hounsfield unit values to materials with chemical compositions and densities appropriate for the tissue types found in the human body. This past year, the performance of the kernel generation code was improved significantly, and the memory requirements reduced, so that simulations can be performed using the full resolution of the CT scanners in clinical use at HUP. The resulting dose kernels thus have resolution equal to that of the CT scanners: 1 mm x 1 mm x 3 mm. The calibration of CT Hounsfield unit to material type and density was improved early this past report year to allow a wider range of tissue densities: the number of density bins for the phantom materials was increased by a factor of 10. Additionally, this past quarter a water equivalent CT calibration was implemented that can be used to investigate some of the shortcomings of Eclipse, which uses water equivalent materials everywhere for its dose calculations. The water equivalent calibration clarifies the origin of some dose inhomogeneities in the Cimmino spot weight optimization code, as described below, but we intend to implement a more suitable CT calibration like that developed by Paganetti et al (Phys. Med. Biol. 53, 2008, p. 4825), which only needs to be adjusted to account for differences between CT scanner hardware and scanning protocol. The file format for Monte Carlo generated kernels files was changed. This permits full-resolution dose kernel data to be written to disk, facilitates parallel calculation of dose kernels, and allowed multi-field spot-weight optimization. The kernel generation code was underestimating the energy needed to reach targets in the patient phantom. This is presently worked around by adding energy layers distal to the PTV, and could be improved further as a student project, by working out a relationship between the particle range in the continuous slowing down approximation, and the depth of the Bragg Peak. Additional spots are also added around the target volume to ensure coverage. Improvements to the spot weight optimization code were necessary mostly to reduce the memory requirement in order to allow multi-field optimization. By improving memory management by our implementation of the Cimmino algorithm, we reduced the optimization time by a factor of 8. We currently require 16 GB of RAM for a two-field optimization using kernels with 1000 protons per spot, which is all the memory available on one of our cluster nodes. We are considering adding memory to our cluster to allow higher resolution spot optimization calculations. We also expanded the dose objective capabilities for the Cimmino optimization: the planner may now specify single-ended inequality constraints in addition to the double-ended inequalities from before. Single-ended constraints are useful to lower the patient integral dose, for example, by specifying that all tissues outside the treatment volume be below some threshold.

Spot weight optimization consists of finding an optimum set of intensities for pencil beams covering the target volume. In Figure II-1 shows two pencil beams of equal intensity delivered to the distal edge of a prostate PTV. In

these figures, the CT data is not overlaid with the dose distributions, although the CT data was used to construct a realistic patient phantom in simulation. The dose distributions for these two pencil beams were obtained by simulating 10000 protons histories for each beam. Relatively, these are very high resolution simulations and take too long and require too much memory to cover an entire treatment volume. The PTV for the prostate case considered here requires at least 1200 spots to cover adequately. Typically we calculate extra spots, about 3000 total, partly due to our poor estimate of the beam range in the patient, so that the spot-weight optimization step has enough spots to cover the target well.
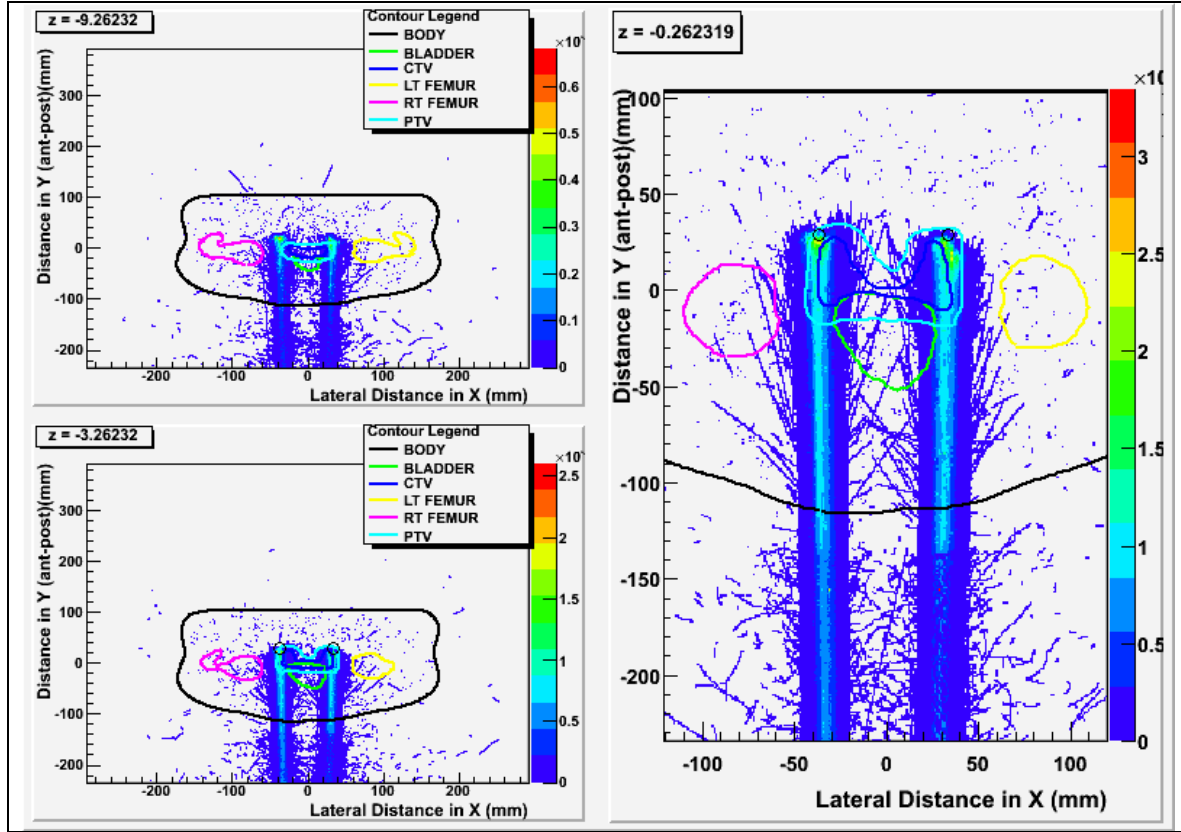

Figure II-1. Dose distribution from two pencil beam spots obtained from Geant4 Monte Carlo simulations, with 10000 proton histories simulated for each spot. The protons were delivered to a voxelized phantom created from a patient CT dataset. The CT data is not rendered in these figures. The structures (physician contoured) indicate the local anatomy.

In Figure II-2, a spot-weight optimization for a prostate case is shown, using kernels with only 100 protons per spot. There are two serious problems: the distal end of the PTV is not covered at all, and the coverage of the proximal end of the PTV is very non-uniform. With respect to the former problem, it was determined that the estimate of the range of the pencil beam, given its energy, in the patient geometry, as defined by the CT dataset and the stopping power calibration curve, is inadequate to predict the position of the Bragg peak. Bragg peaks systematically fall short of their targets by as much as a centimeter in this case. This was shown previously and is repeated here in Figure II-3. The pencil beam targets are indicated with circles. The red circles have been turned off by the Cimmino algorithm, because they are depositing dose proximal to the PTV. The targets indicated by black circles receive dose, but it can be seen that their dose falls too shallow of the target. Targets on additional energy layers were added to the list of kernels generated by simulation. That ensures coverage of the PTV, at the cost of some additional kernels being calculated. The result is dose coverage like that shown in Figure II-4. The PTV is now covered by dose all the way to the distal end. The spot weight optimizer has even more kernels distal to the target, but it has turned those off because they do not improve the PTV dose uniformity. This additionally serves as a check that the optimizer is on the right track.
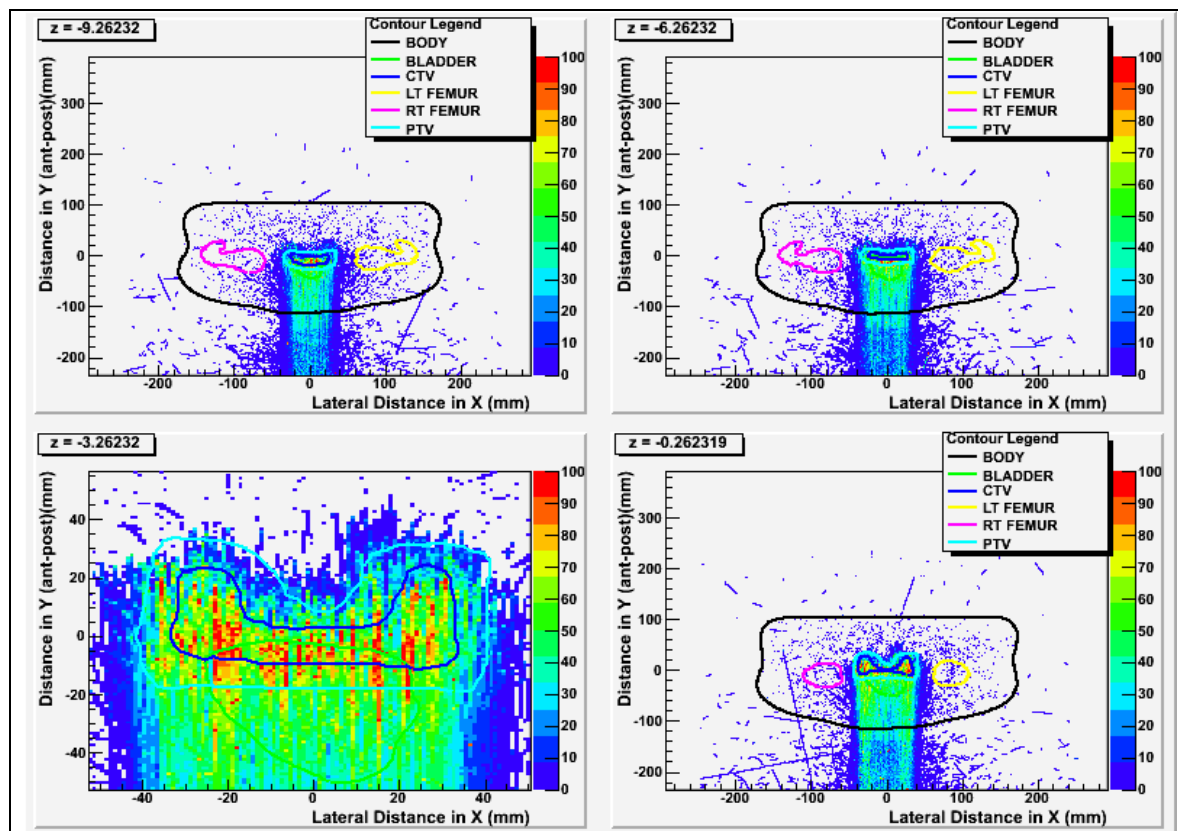
18

Figure II-2. A pencil-beam prostate treatment plan (IMPT) obtained using the Cimmino algorithm to optimize the intensity of 1200 pencil beam dose kernels generated with Geant4 Monte Carlo simulation. This optimization attempted to cover the PTV volume with a dose between 100 and 102 Gy. The distal end of the beam does not receive adequate dose, because the pencil beam energy needed to reach the targets covering the PTV is underestimated.
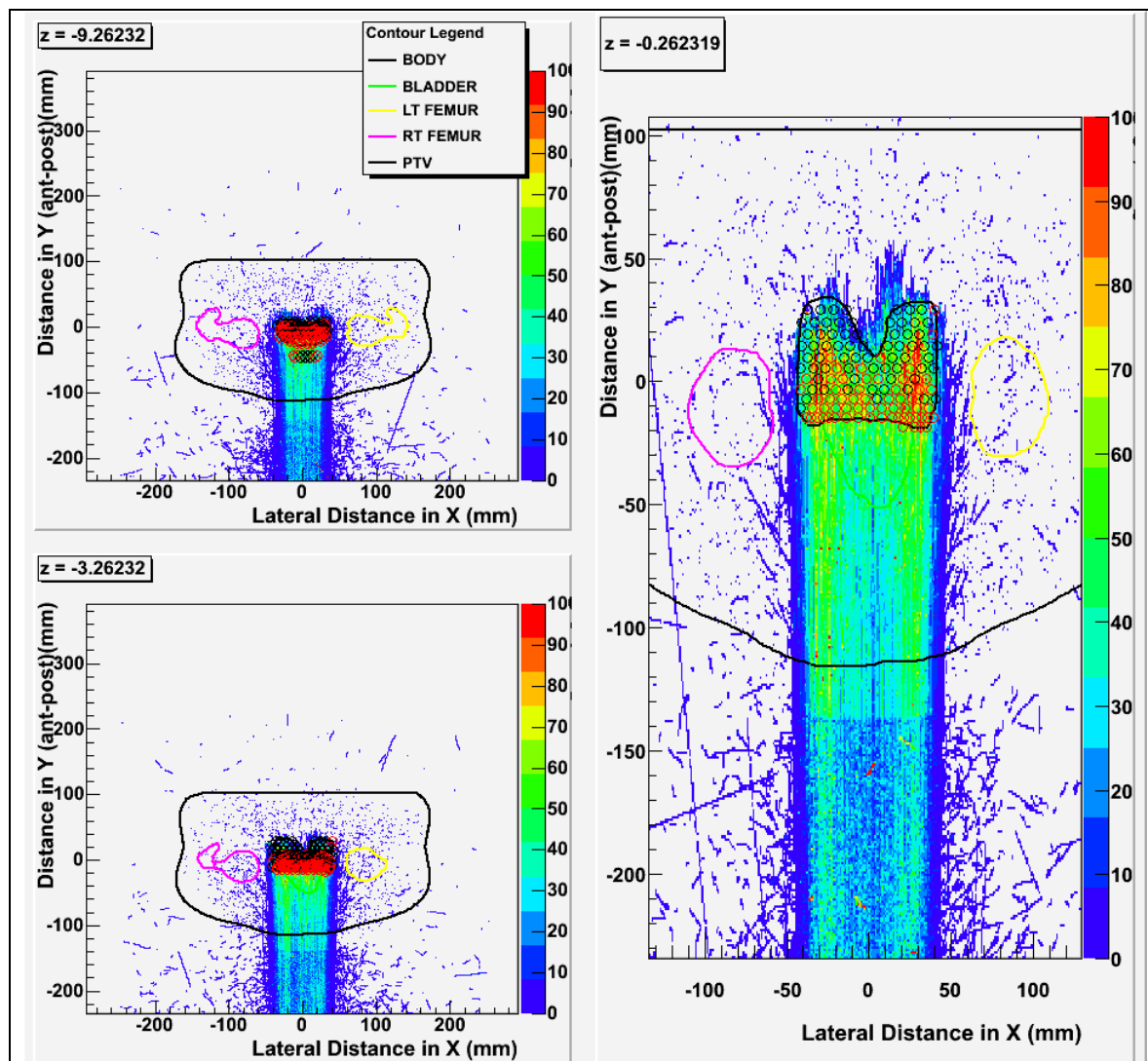
Figure II-3. An IMPT plan with the pencil beam targets indicated with circles. Red circles indicate targets that were turned off (zero intensity) by the Cimmino optimization. The dose from each pencil beam is actually deposited more proximal to the target points, so that the deepest targets (black circles) are responsible for the (too proximal) dose distribution.
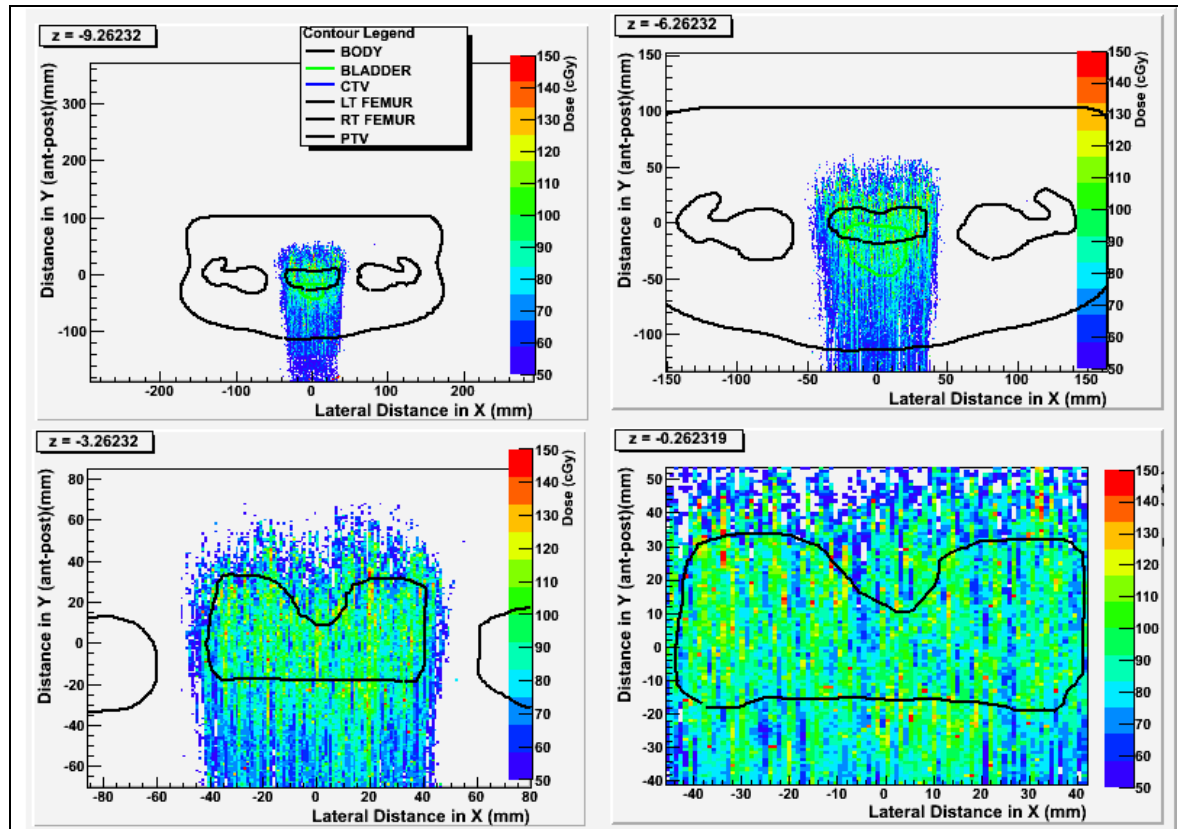
Figure II-4. IMPT plan with additional higher energy layers added to cover the distal end of the target. The coverage is not uniform (+/- 50%) because the number of protons simulated for each target in the PTV is only 100.

The dose uniformity to the PTV in Figure II-4 is still not good. Dose in the PTV varies by +/- 50% of the target dose (100 Gy). It was determined that this is due to large statistical noise present in each pencil beam kernel, because only 100 primary protons were simulated for each pencil beam. The dose kernel for two pencils beams with only 100 protons each is shown in Figure II-5. Compared with the same kernels at 10000 protons per spot (Figure II-1), it is clear that only 100 protons is not enough to get the mean dose to the voxels of the patient phantom with enough accuracy. A study was done to find a suitable number of protons per spot, and eventually a value of 1000 was selected. In Figure II-6 we show the transverse dose profile for a single pencil beam, through the Bragg peak, and the uncertainty (standard deviation of the mean) along the same line. Far in the penumbra of the pencil beam, at the 2% dose level, the dose is determined to an accuracy of 2%, relative to the dose at that point (2% of the maximum). We think this accuracy is enough to resolve the penumbra very well. At 1000 protons per spot, each spot takes about 30 seconds of simulation, so that kernels for a PTV with a typical 3000 targets takes about 24 hours on a single CPU. This is too long for routine clinical use, but could be improved by calculating the kernels in parallel using more CPUs.
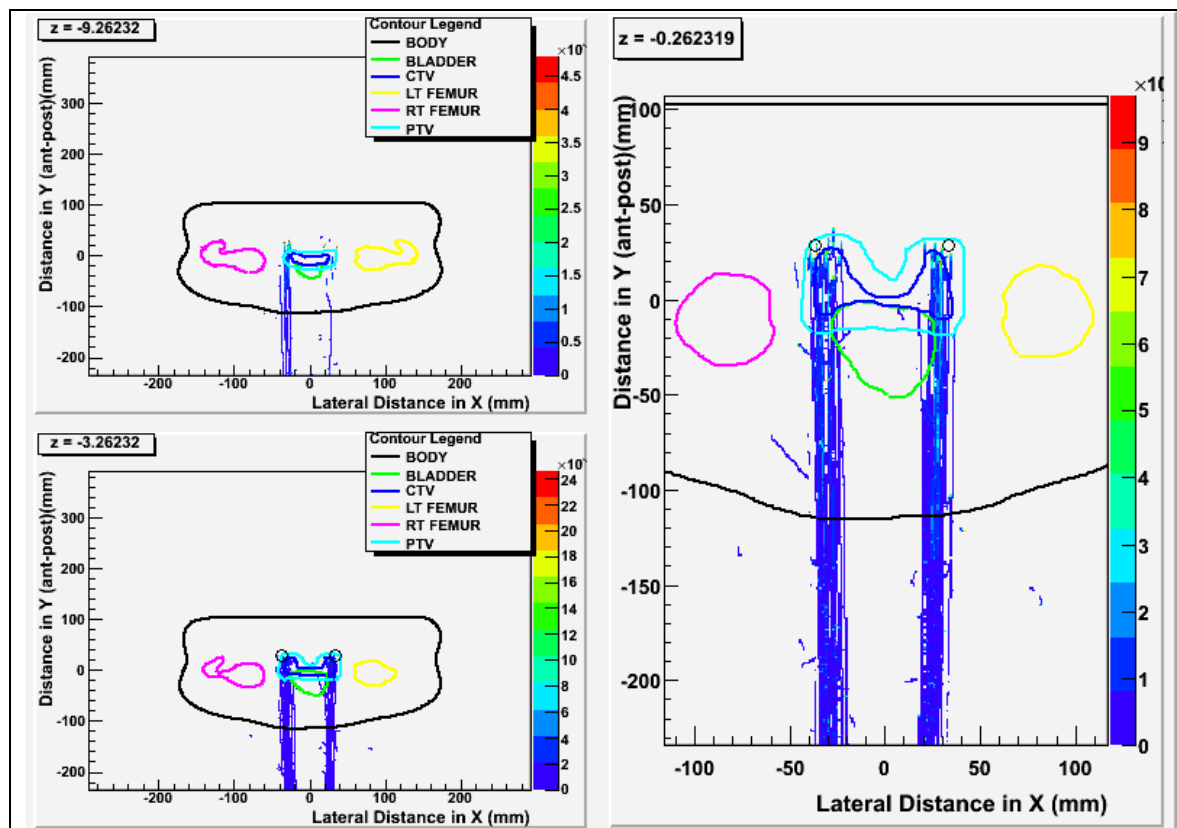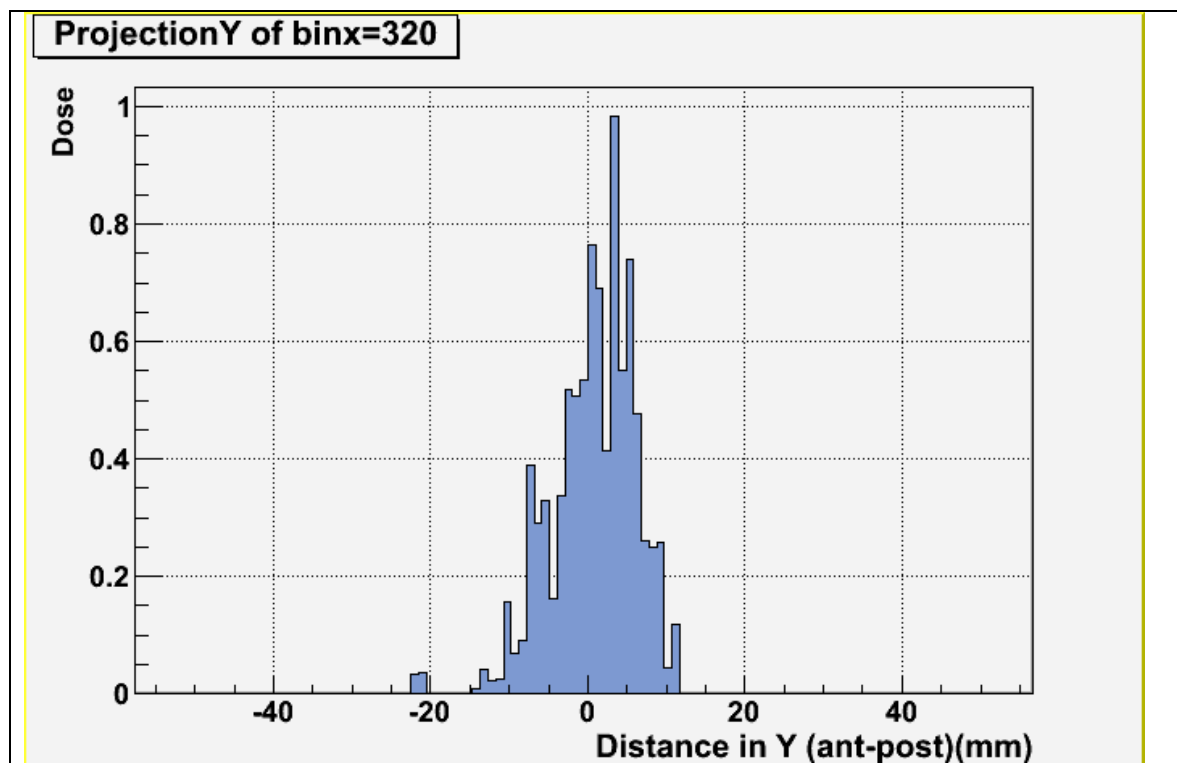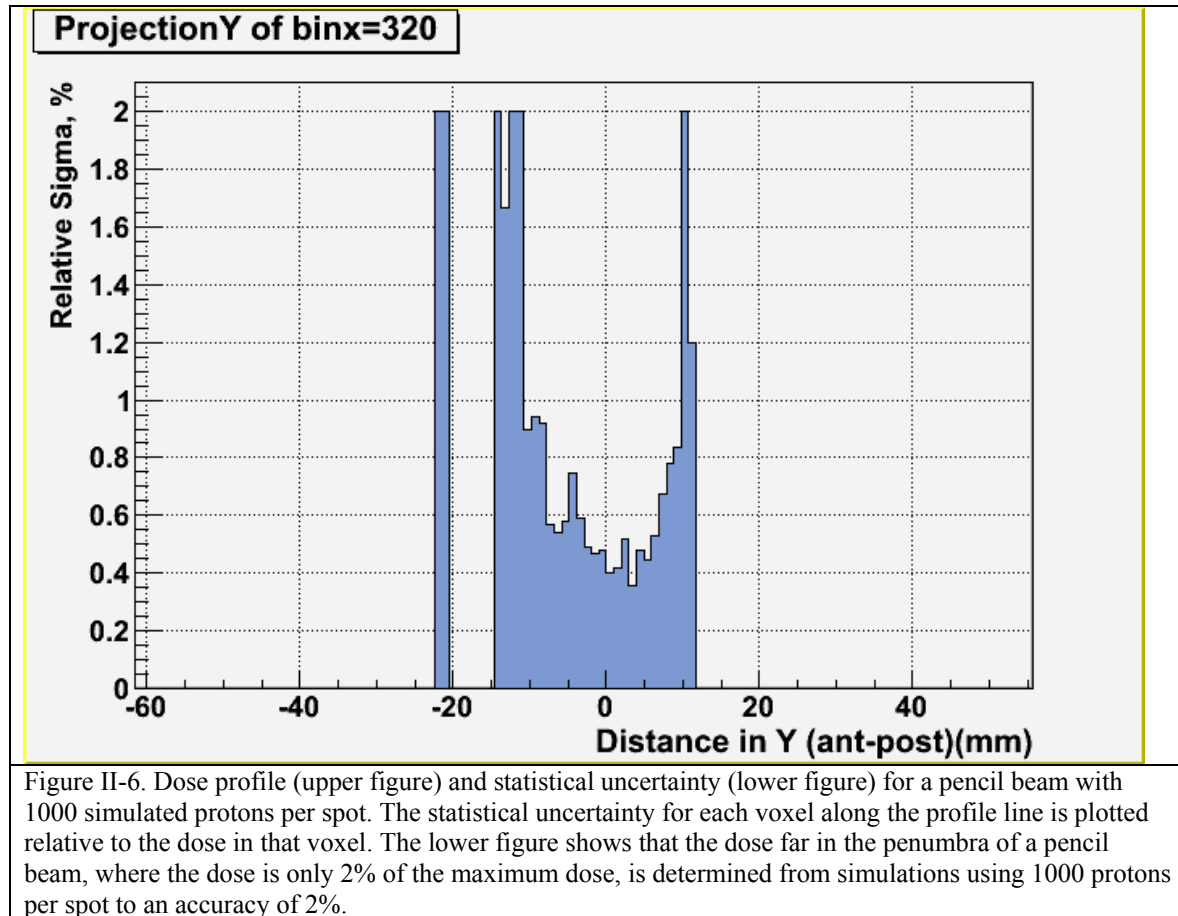
Figure II-5. Two pencil beams simulated with 100 protons per spot. Compare with Figure II-1, where 10000 spots were used.

Figure II-6. Dose profile (upper figure) and statistical uncertainty (lower figure) for a pencil beam with 1000 simulated protons per spot. The statistical uncertainty for each voxel along the profile line is plotted relative to the dose in that voxel. The lower figure shows that the dose far in the penumbra of a pencil beam, where the dose is only 2% of the maximum dose, is determined from simulations using 1000 protons per spot to an accuracy of 2%.

The plan shown in Figure II-7 was optimized using kernels with 1000 protons per spot. Uniformity of dose to the PTV is now +/- 15%. The dose scale was adjusted for Figure II-8 in order to better demonstrate a hot spot outside the PTV. This spot was used by the optimization to improve coverage within the PTV near its proximal edge. There was no penalty for dose to tissue outside the PTV for this optimization. The capability was added to our Cimmino implementation to allow specification of single-ended inequality constraints, so that we could request, for example, that the dose to voxels outside the PTV be less than a threshold.
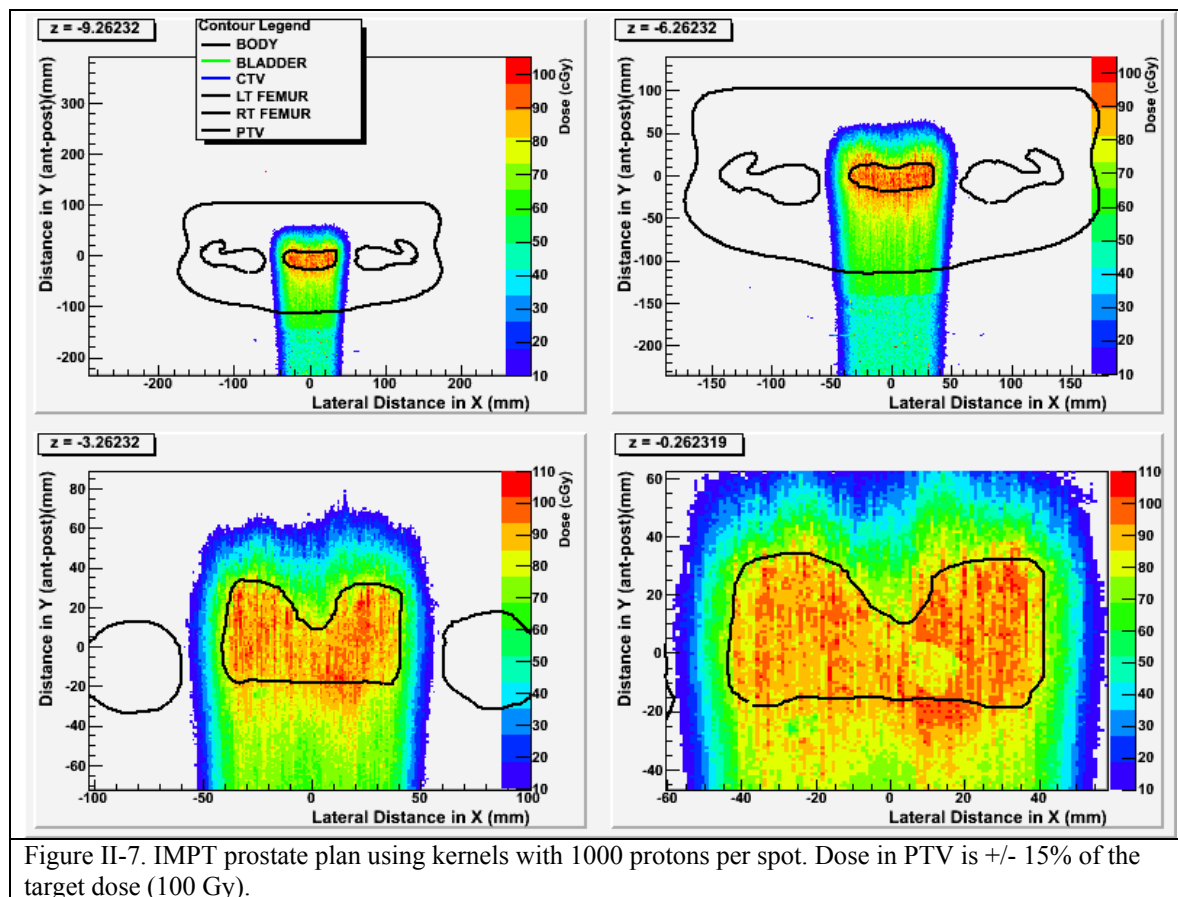
Figure II-7. IMPT prostate plan using kernels with 1000 protons per spot. Dose in PTV is +/- 15% of the target dose (100 Gy).
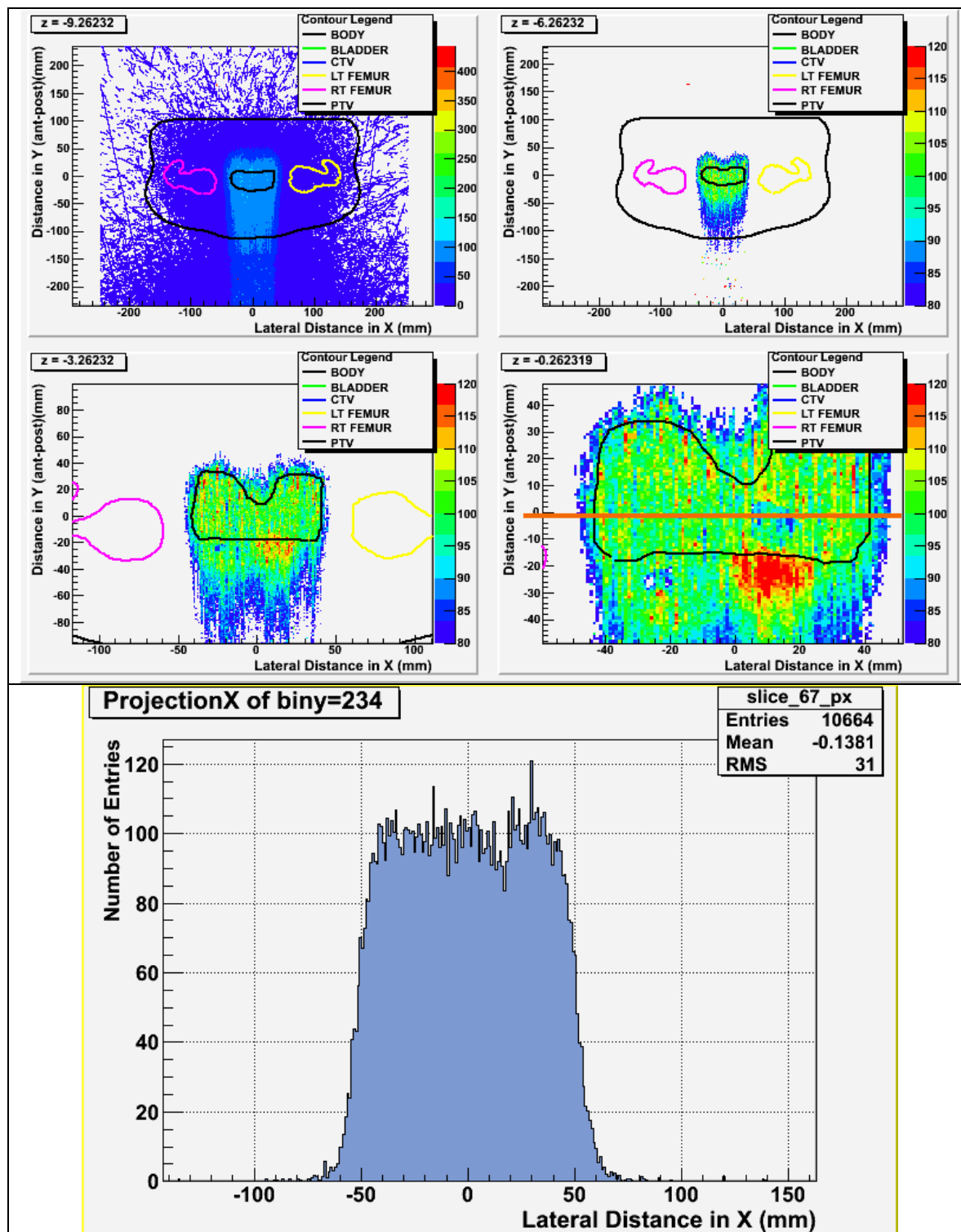
Figure II-8. IMPT prostate plan, similar to Figure II-7, but with a narrower color scale showing more clearly the uniformity of the dose to the PTV. The intensity of the hot (red) spot proximal to the PTV was used by the optimization to increase the dose to the proximal edge of the PTV above 100 Gy. There was no penalty for dose to tissues outside the PTV in this case. The lower panel is the dose profile along the line shown (y = -2 mm, z = -0.26 mm)

Figure II-9 is a plan obtained using a single-ended constraint of dose to tissue outside the PTV <= 80 Gy, in addition to the PTV constraint of 100 <= PTV <= 102 Gy. The hot spot from Figure II-8 is eliminated.
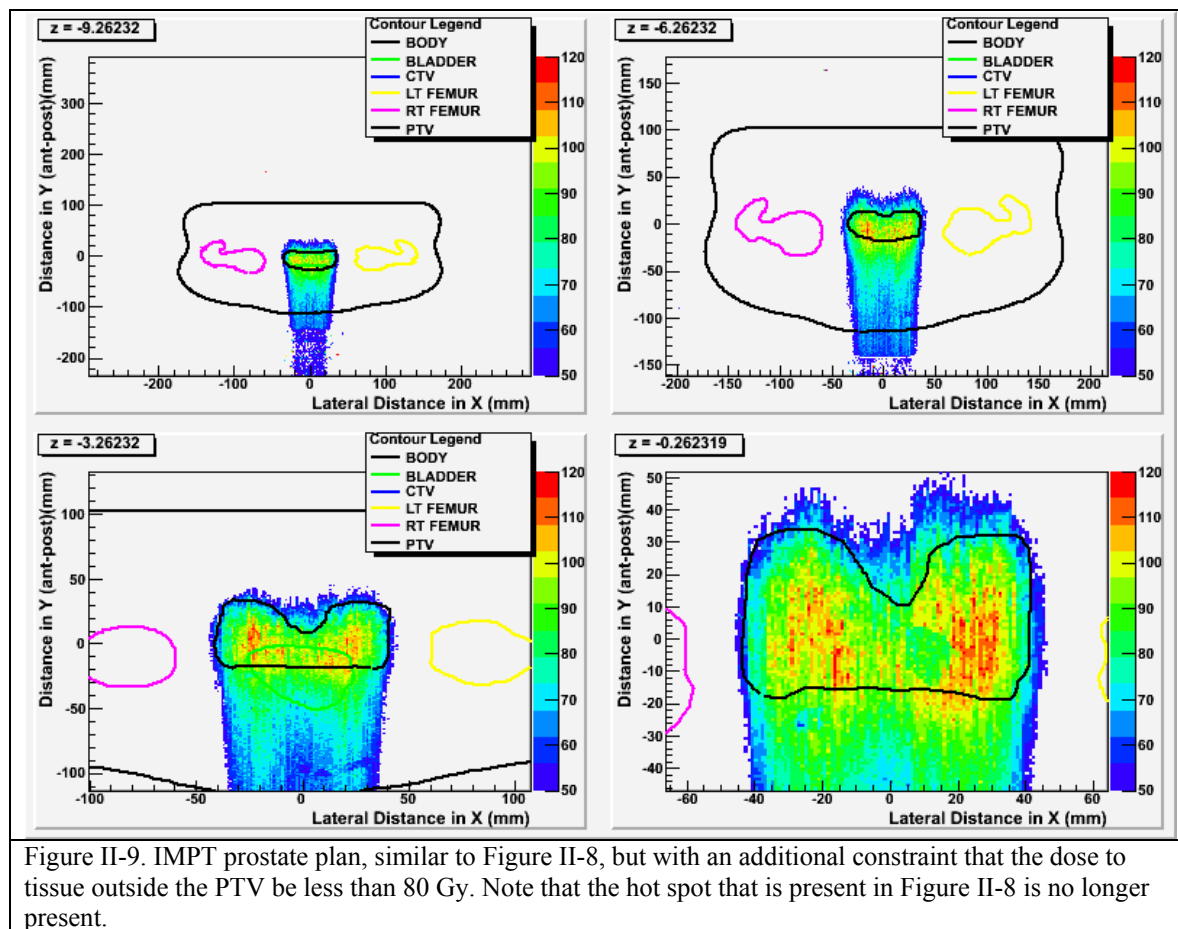

Figure II-9. IMPT prostate plan, similar to Figure II-8, but with an additional constraint that the dose to tissue outside the PTV be less than 80 Gy. Note that the hot spot that is present in Figure II-8 is no longer present.

The Cimmino optimization for the single-field prostate plans with 1000 protons per spot takes about an hour to converge. It requirse about 500 iterations, (each iteration involves projections onto all the constraint subspaces) for convergence, as indicated in Figure II-10.

Figure II-10. Convergence of the Cimmino spot-weight optimization algorithm for the single-field IMPT prostate plans shown in previous figures. The optimization converges after about 500 iterations, which takes 3 hours.
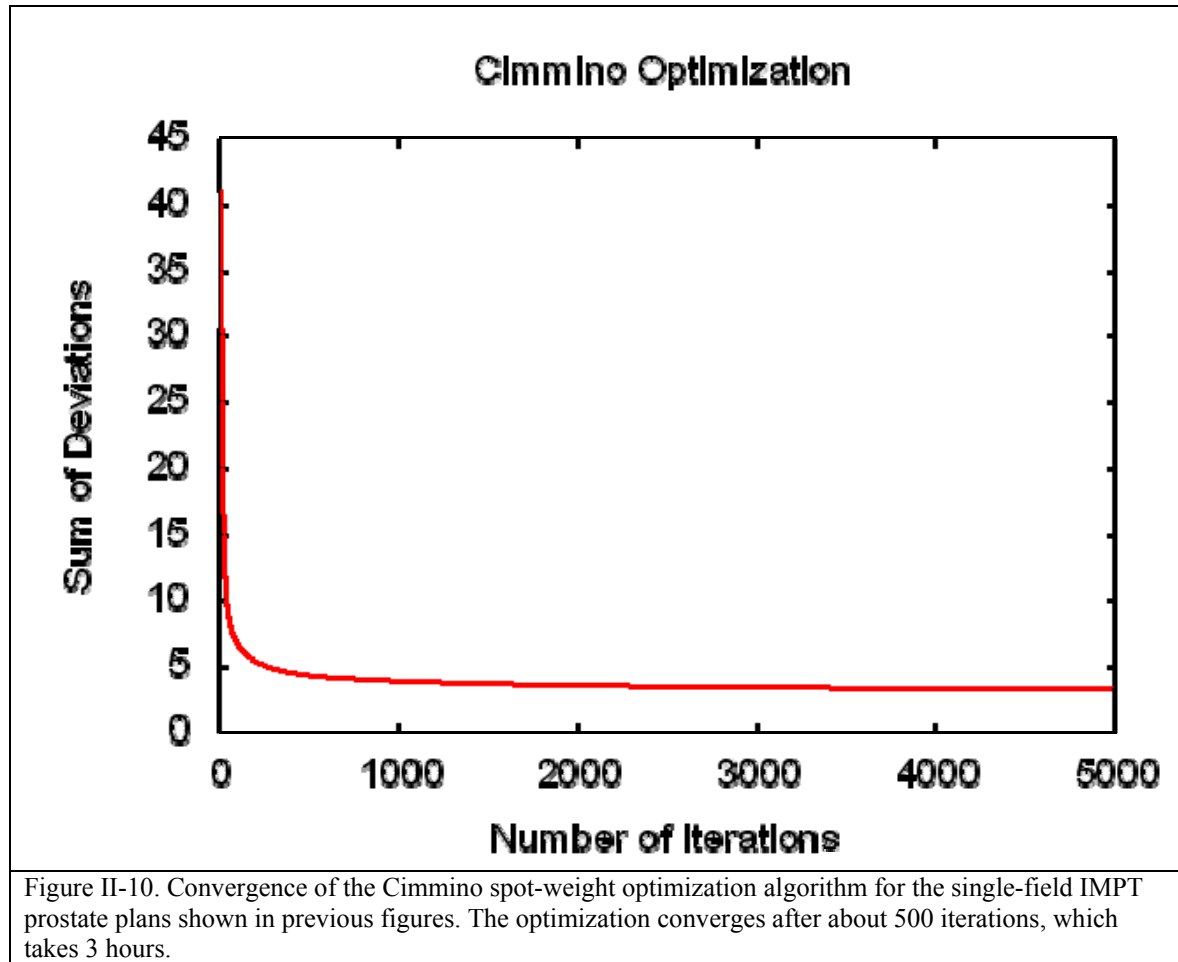
Figure II-11 is a more realistic two-field proton plan, optimized using our Cimmino implementation. This optimization gave a cold spot in the PTV, which appears yellow in the lower right dose slice of Figure II-11. Also shown is a line profile of the dose through the cold spot. The optimizer has turned up the intensity of spots to that region, resulting in a hot ring around the cold spot. It was determined that the Hounsfield unit values corresponding to the voxels in the cold spot are higher (greater than 50) than the rest of the PTV. The stopping power calibration is plotted in Figure II-12. The calibration in use is the calibration contained in the Geant4 DICOM example code, but with a factor of ten higher density resolution. The full range of Hounsfield units is divided into 10 subranges, and a unique material composition is assigned to each subrange. The density also varies as a function of the Hounsfield unit, with a unique density for each HU value. When the proton stopping power that results from the Geant4 example calibration is plotted, it can be seen that there are discontinuities in the stopping power curve. The discontinuity at about HU = 50 is responsible for the cold spot in Figure II-11. The material in the cold spot has a lower stopping power than the surrounding tissue, so the dose deposited there is lower. The CT dataset was examined, and there is no anatomical feature corresponding to the cold spot. In this case, the cold spot is an unrealistic artifact resulting from the stopping power calibration.
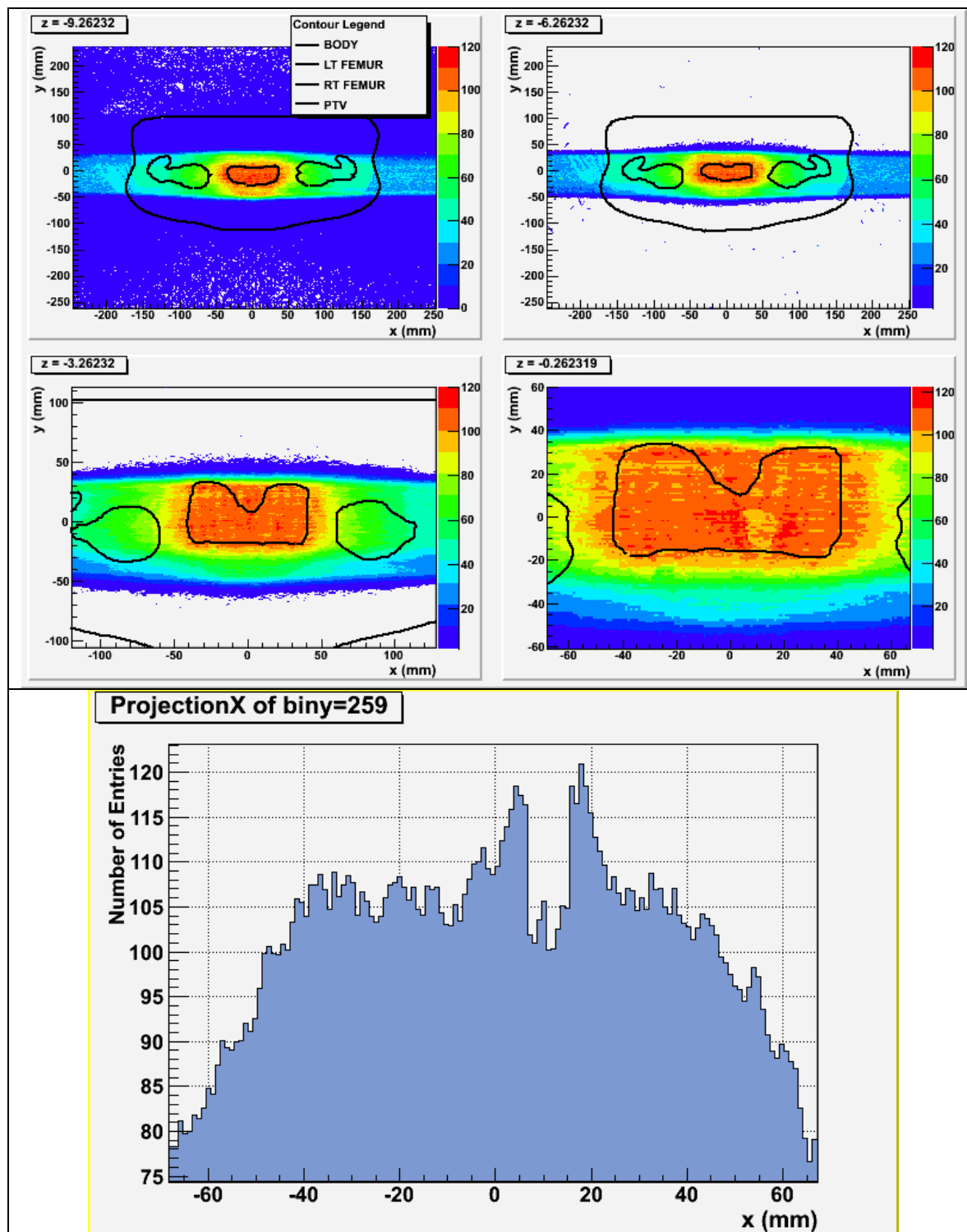
Figure II-11. Two-field IMPT prostate plan. In the lower-right slice of the dose colorwash (upper figure), a cold spot (yellow) can be seen in the PTV. The lower figure is a dose profile through the cold spot (at y = -5 mm). The spot size is 1 cm FWHM at this depth. The intensity of spots near the cold spot have been increased by the optimization in order to bring the dose closer to prescription (100 Gy), resulting in a hot ring balanced by a cold center of dose. The center is cold because of a discontinuity in the HU-to-stopping-power calibration curve (see Figure II-12).
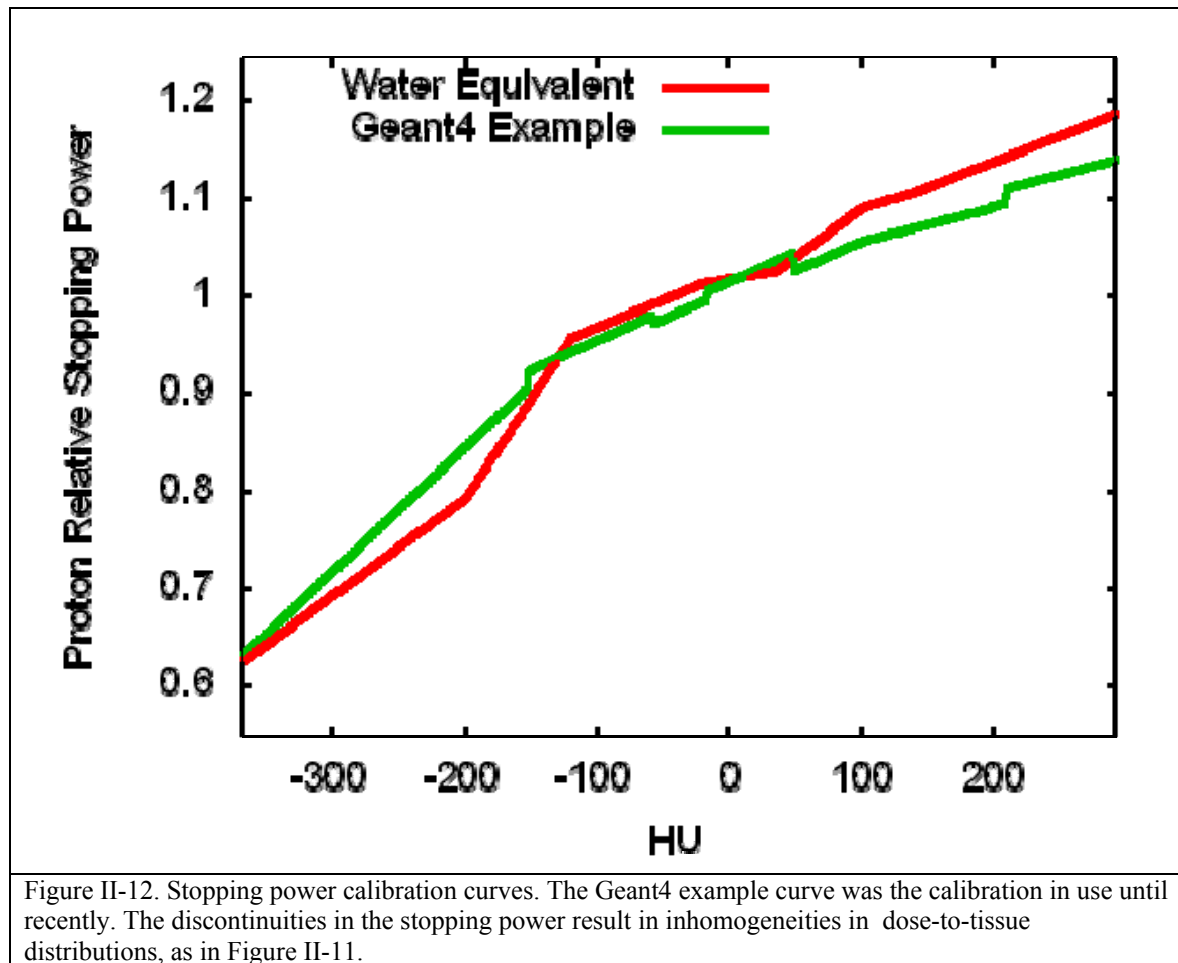
Figure II-12. Stopping power calibration curves. The Geant4 example curve was the calibration in use until recently. The discontinuities in the stopping power result in inhomogeneities in dose-to-tissue distributions, as in Figure II-11.

A water equivalent stopping power calibration was implemented, in part to verify that the cold spot in Figure II-11 is resolved. The two calibrations are illustrated in Figure II-13. The water equivalent calibration could also be used to determine the effect of ignoring material inhomogeneities in the patient, as is done by Eclipse. Comparision studies could be done between a water equivalent calibration and a calibration using different material types, such as the calibration published by MGH (Paganetti et al, Phys. Med. Biol. 53, 2008, p. 4825). That calibration is based on the a stoichiometric method published by Schneider, Bortfeld, and Schlegel in 2000. We have performed a stoichiometric calibration following their procedure to obtain the stopping power calibration for our treatment planning system. The results of our calibration are compared with the MGH group's results in Figure II-14. The MGH group calibration would not be appropriate for our CT scanners and our scan protocol: at HU = 400, for example, the oxygen fraction would be underestimated by the MGH calibration, and the carbon fraction would be overestimated. The differences are likely due to differences in the CT scanners and operating parameters between HUP and MGH, such as the beam energy characteristics.
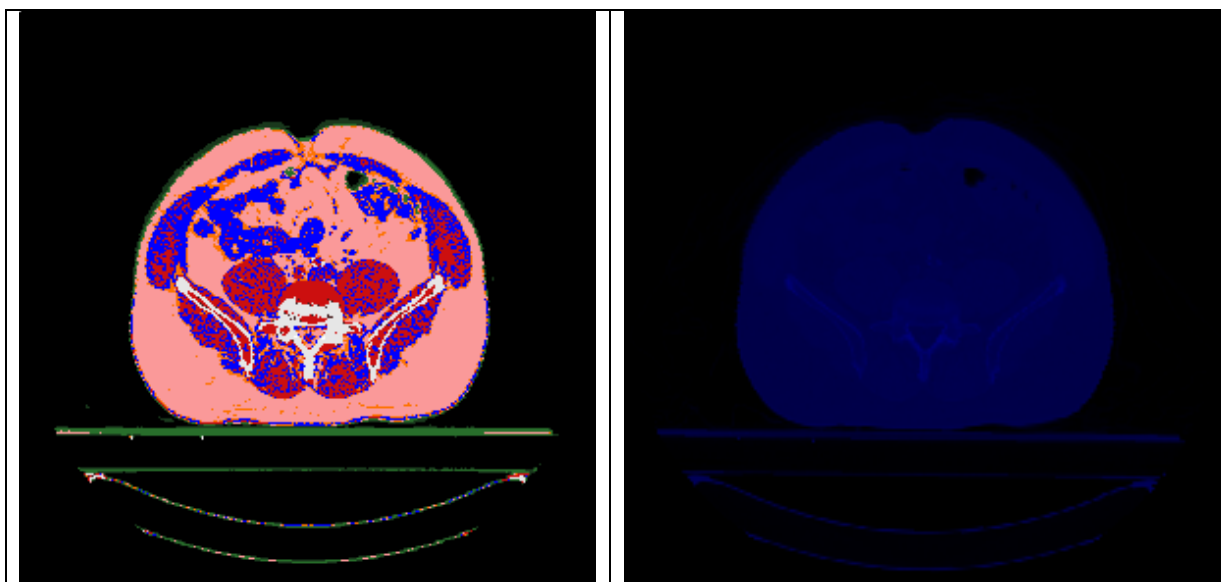
Figure II-13. Material maps for the two calibration curves in Figure II-12. On the left is the Geant4 example calibration. Different colors correspond to different tissue types, which have different chemical compositions. On the right is the recently-implemented water-equivalent calibration, which matches the calibration used by the dose algorithms in the Eclipse treatment planning system, but is physically less realistic. In both calibrations, the density of the materials vary continuously as a function of the Hounsfield unit.
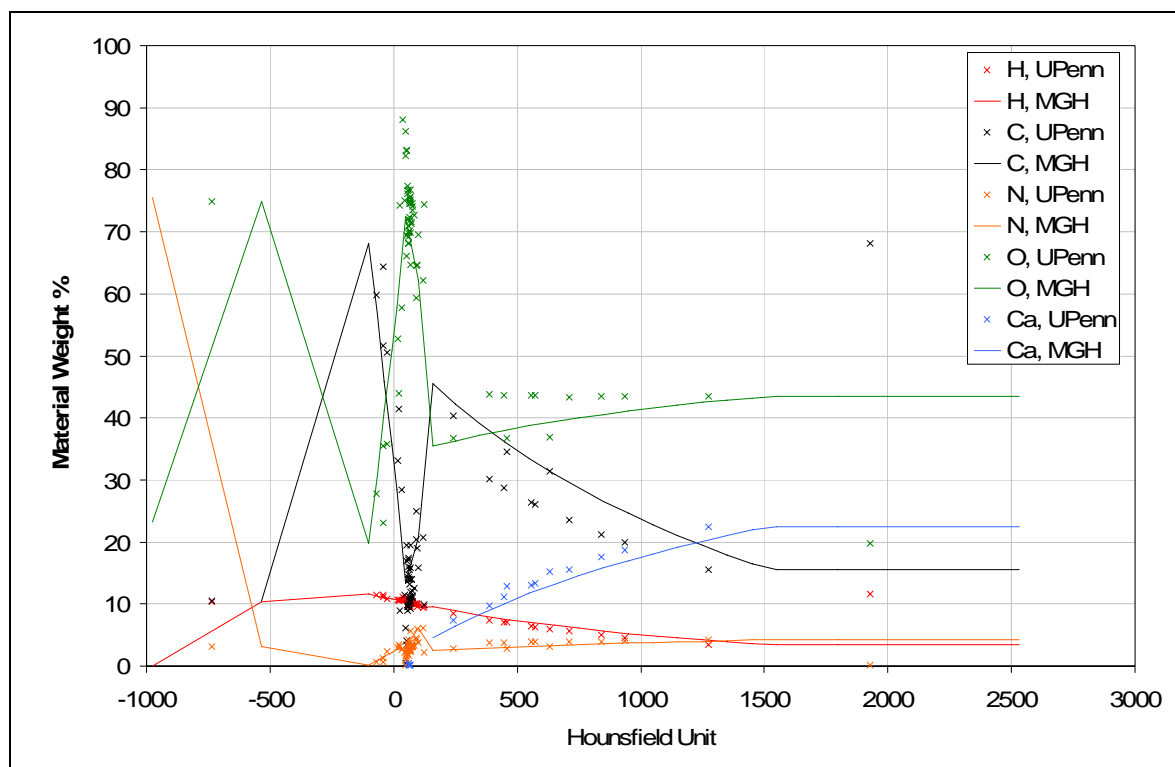

Figure II-14. Comparison of the stopping power calibration curves in use at MGH, versus that obtained using the CT scanners at HUP and the stoichiometric calibration method of Schneider, Bortfeld, and Schlegel (2000).

Using the water-equivalent calibration, we find an improved dose homogeneity to the PTV, as shown in Figure II-15. The coverage to the PTV for the plan on the left is very good, with the entire PTV receiving >= 80 Gy as prescribed. The other plans show the effect of increasing the priority of a maximum dose objective for the tissue outside the PTV. An objective that dose outside the PTV be <= 50 Gy was included in the optimization, and the priority successively increased. The dose to femoral heads should typically be kept below 50 Gy. Increasing the priority of the normal tissue objective lowers the dose to the femoral heads, at the cost of some of the PTV periphery does not receive the full prescription dose.
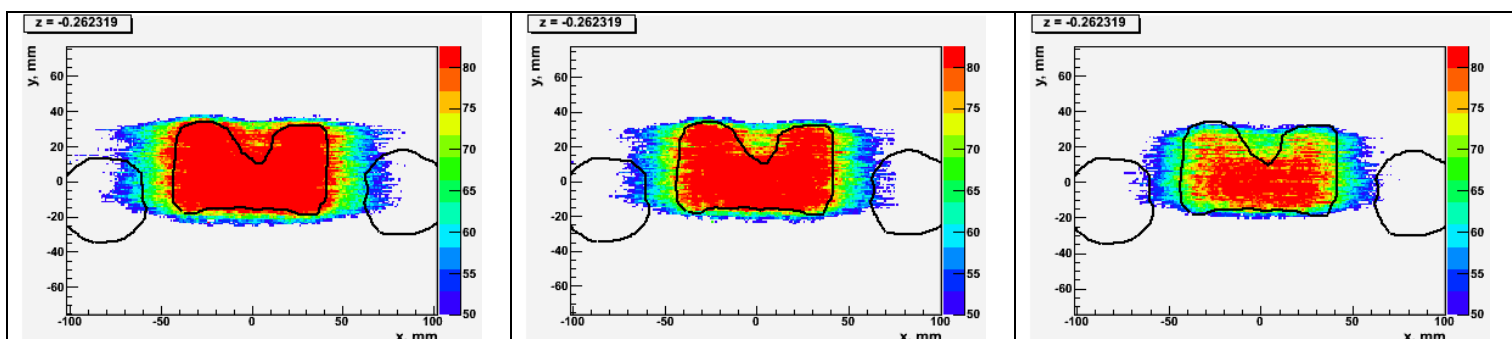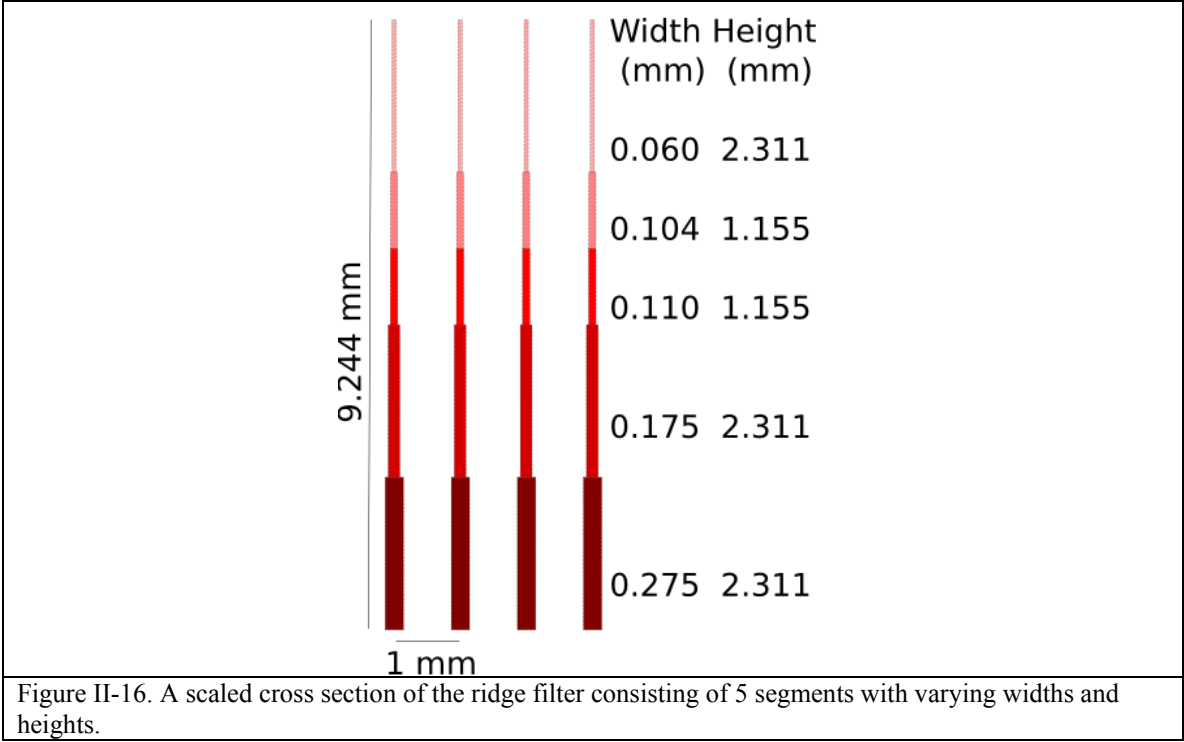

Figure II-15. For a two-field IMPT prostate plan, effect of the priority parameter for dose constraints. Each optimization has PTV >= 80 Gy and other tissue <= 50 Gy objectives. On the left, the priority of the other tissue objective is 0.01 (relative to the PTV objective), in the middle the priority is 0.1, and on the right the priority is 1 (same priority as the PTV objective). The dose to the femoral heads can be reduced by increasing the priority of the body dose objective, at the cost of poorer PTV coverage: the dose to the periphery of the PTV on the left is the full prescription dose (80Gy), in the middle it is 75 Gy, and on the right only 65 Gy.
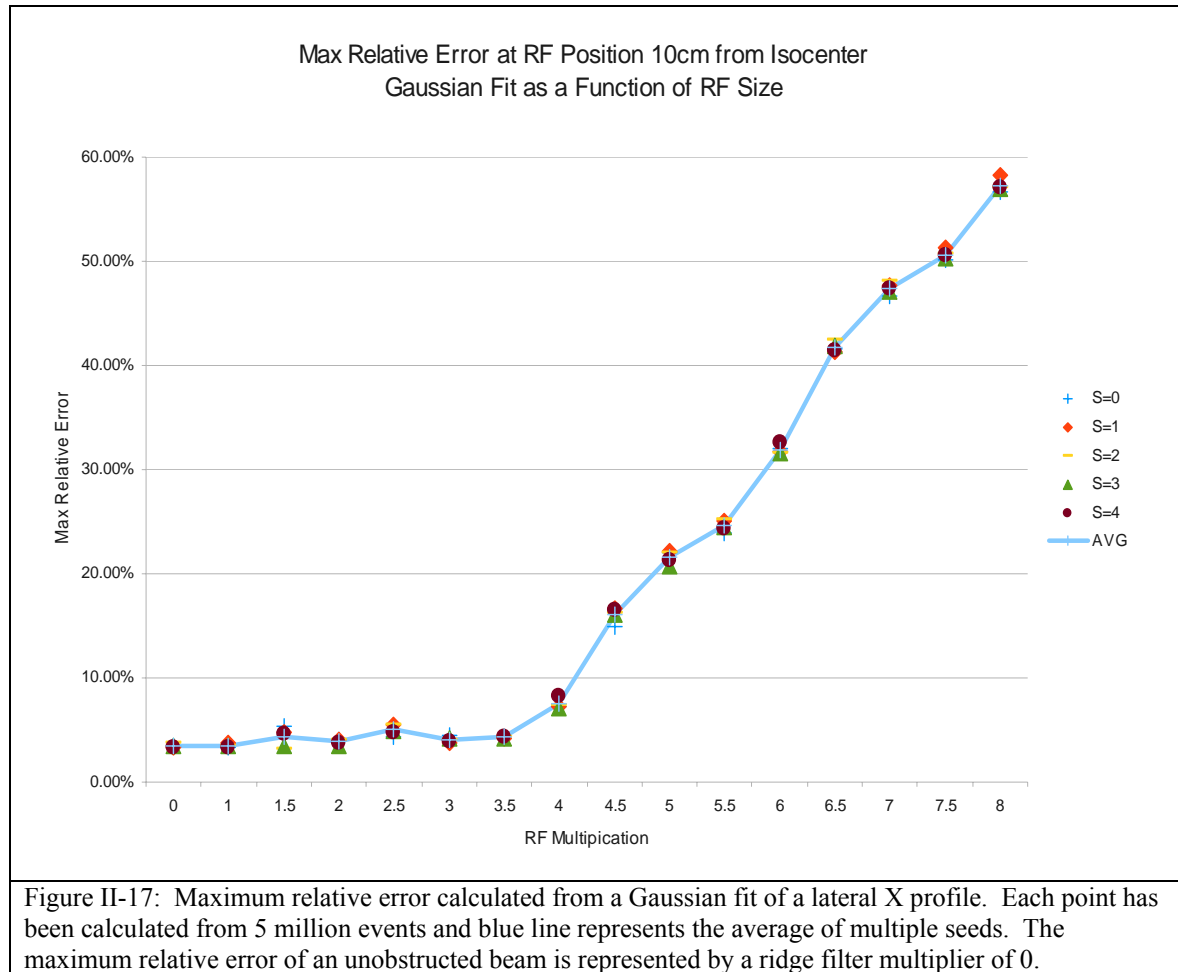
For next quarter, Derek will continue to work towards simulations incorporating patient motion, using 4D CT datasets.

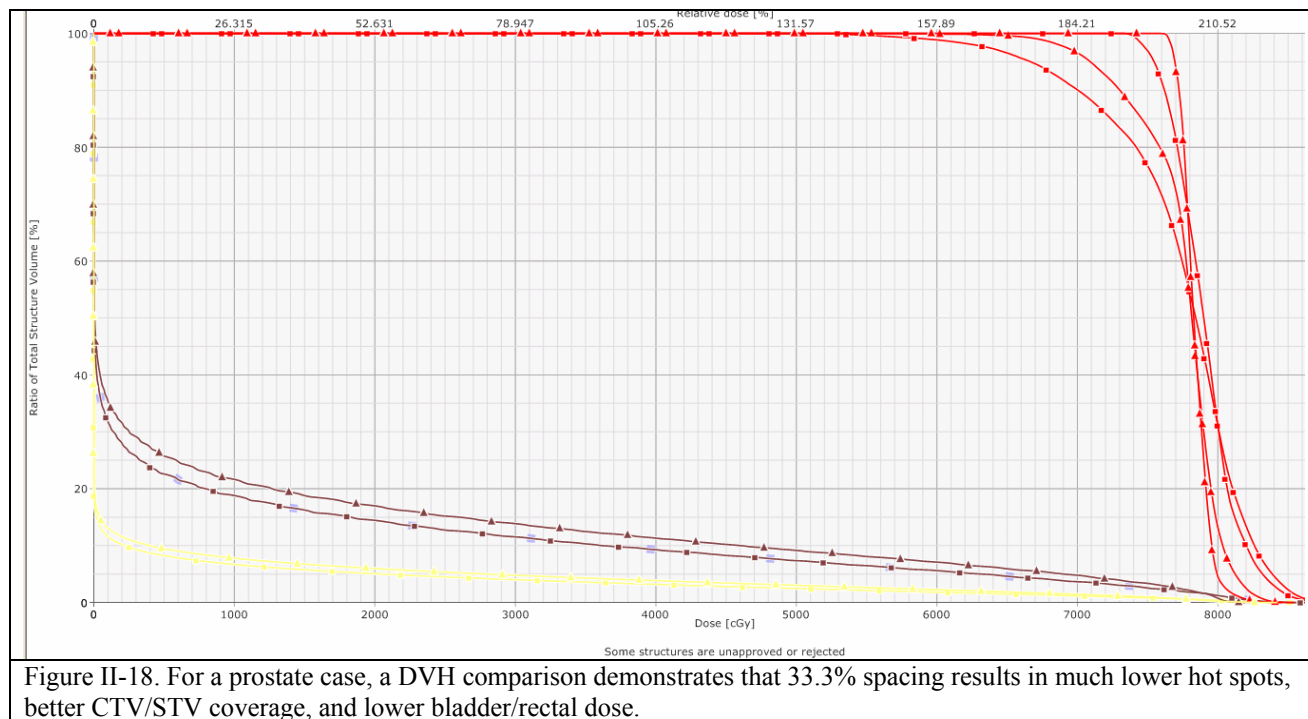*Development of Range Shifter and Ridge Filter*

This past year, James Durgin studied methods for treating shallow tumors with pencil beam scanning. He simulated range shifters for shallow depths, and investigated the effect of different materials and different mounting positions on the beam penumbra. James also simulated ridge filters to spread out the Bragg peak, which can be quite narrow at shallow depths. James has commissioned our Eclipse treatment planning system with simulated commissioning data, so that we can plan cases with the beam modification devices and draw conclusions about their effectiveness and suitability for different disease sites. Comparison plots of the penumbra for

James arrived at a design for a ridge filter that produces a flat spread out Bragg peak (SOBP) of about 8 mm width. The design was reported previously, but is shown again here in Figure II-16 This design is difficult to machine, because of the ridges with thicknesses less than 100 um. It is really the ratio of the width of each ridge to the width of the entire pattern that is responsible for creating the flat SOBP. That is, the entire design can be scaled in the dimension of the filter widths, as long as the scale of the filter remains small compared to the size of the beam spot that strikes the ridge filter, to avoid having any shadow from ridge filter in the dose distribution. James looked at the dose profile for pencil beams delivered through the ridge filter design of Figure II-16 with the lateral dimensions scaled by a parameter s, labeled "RF Multiplication" in Figure II-17. With a scaling of about 4 or larger, one can start to see a shadow left by the ridge filter in the beam profile. The factor of 4 is valid for a ridge filter mounted close to the patient. Because additional lateral scatter smears the shadow, James found that for a ridge filter mounted 50 cm from isocenter, a scaling factor of 6 produced a good profile. Thus, a ridge filter with smallest ridge dimension about 250 um could be used to produce an SOBP in our beam line, and can probably be machined on the milling machine that produces our compensators. We are now pursuing the manufacture of a prototype with our machinist.

Figure II-16. A scaled cross section of the ridge filter consisting of 5 segments with varying widths and heights.

Figure II-17: Maximum relative error calculated from a Gaussian fit of a lateral X profile. Each point has been calculated from 5 million events and blue line represents the average of multiple seeds. The maximum relative error of an unobstructed beam is represented by a ridge filter multiplier of 0.
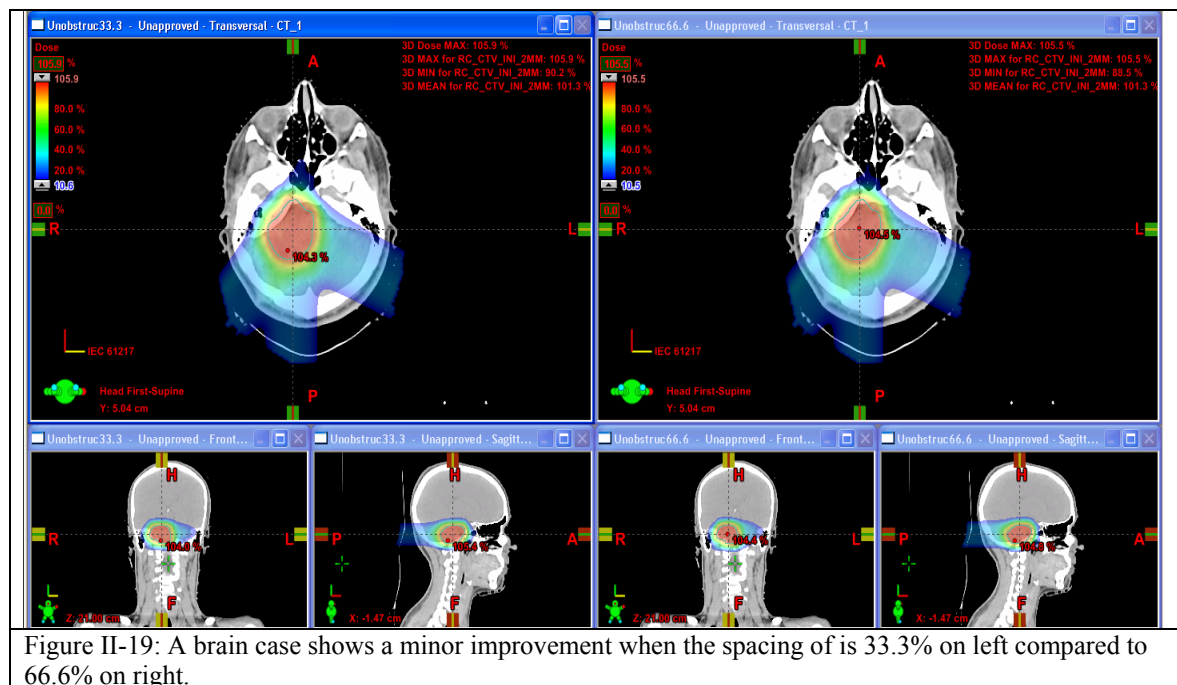
Test treatment plans were generated to determine coverage for a prostate and brain case. These test plans were used to determine the clinical impact of various configuration parameters including use of range shifters/ridge filters, lateral spot spacing, and energy layer spacing. The initial configuration using an unobstructed beam, lateral spacing of 66.6%, and energy layers of twice the next highest range sigma yielded a poor lateral-opposed prostate patient plan with significant dose variation within the target. This variation was a result of lateral spacing, as the treatment planning system only used three lateral positions to cover the target in a given image slice. Previous research had indicted that a spacing of approximately two-thirds is ideal, but this was using the assumption that all in-plane spots had an equal weight. In reality, relatively few spots are given a high weight on the border of the target with reduced weighting on the inside. Decreasing lateral spacing to 33.3% provided the treatment system with more options for beam placement in resulted in higher quality plans.

Figure II-18. For a prostate case, a DVH comparison demonstrates that 33.3% spacing results in much lower hot spots, better CTV/STV coverage, and lower bladder/rectal dose.

Decreasing lateral spacing also improved the 3-field brain tumor case, although to a much less extent. While the 33.3% lateral spacing offered modest improvements, the total number of spots increased by a factor of 2.5. Assuming a ~5 ms switching time between spots, this would represent an increase in treatment time of approximately 10 seconds per day of treatment.

Figure II-19: A brain case shows a minor improvement when the spacing of is 33.3% on left compared to 66.6% on right.

While the relatively few highly-weighed spots may mean that more lateral spots are needed, it also provides an opportunity to reduce the number of energy layers. One option is the IBA ridge filter. Using energy layer spacing of twice range sigma, the parallel opposed beams for the prostate case each required 25 energy layers for the unobstructed beam. With the IBA ridge filter, this decreased to 21 energy layers. The ridge filter also introduced lateral scattering, which decreased the total number of spots from 4481 to 3687 and as a result reduced plan quality.

For a shallow brain case, a 7.5 cm water equivalent range shifter showed promise over an unobstructed beam. The use of the range shifter decreased energy layers by ~35% both per field and total energy layers per plan. In this particular case, the range shifter would have decreased treatment time by approximately 1.5 minutes per day of treatment assuming 3 seconds to switch between energy layers.

One can also manually input energy layer spacing parameters into the beam configuration software. Using energy layer spacing of fixed 0.5 or 1 cm layers resulted in comparable plans, while reducing energy layers and total spots. For the prostate plan using IBA's ridge filter with energy layers spaced by 1 cm, total energy layers were reduced from 50 to 18, and total spots from 4481 to 1684 compared to an unobstructed beam with spacing determined by twice range sigma.
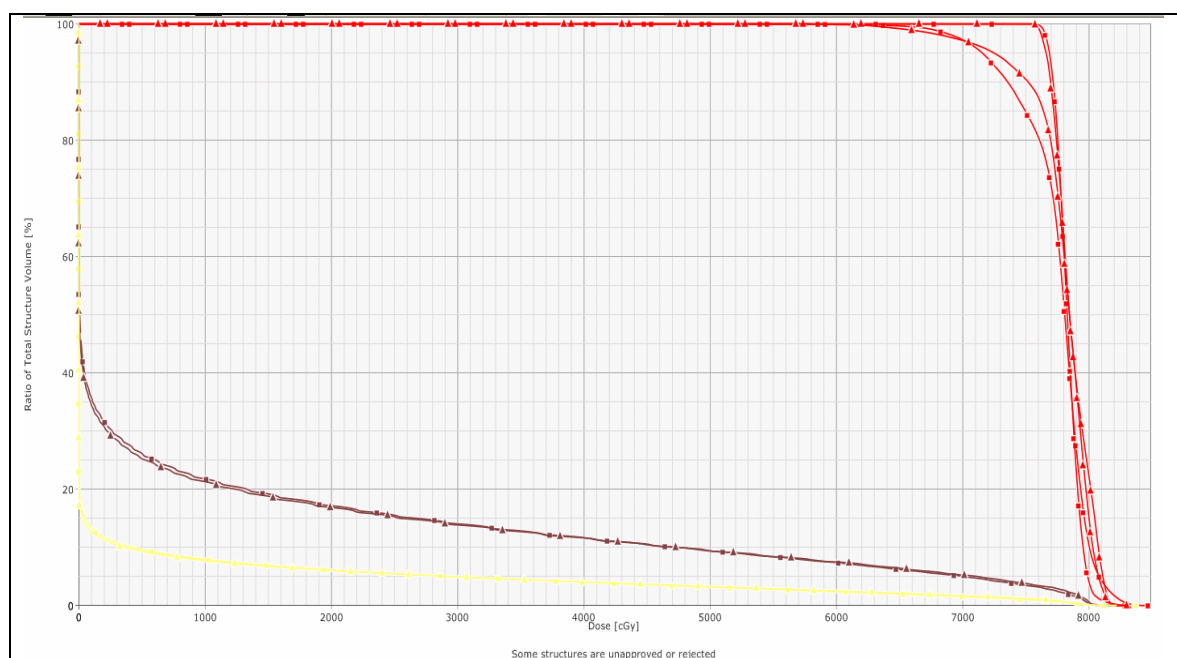

Figure II-20. For prostate plans, defining an energy layer spacing of 1 cm resulted in similar CTV, bladder, and rectal coverage compared to an unobstructed beam with energy layer spacing of twice range sigma. STV coverage is reduced for the fixed 1 cm spacing, and total time saved is approximately 110 seconds per day of treatment.

.

For the brain case, energy layer spacing of 1 cm with the unobstructed beam resulted in noticeable beam spots within the target volume. With the range shifter in place, however, 1 cm spacing is comparable to twice range sigma and an acceptable plan is generated.
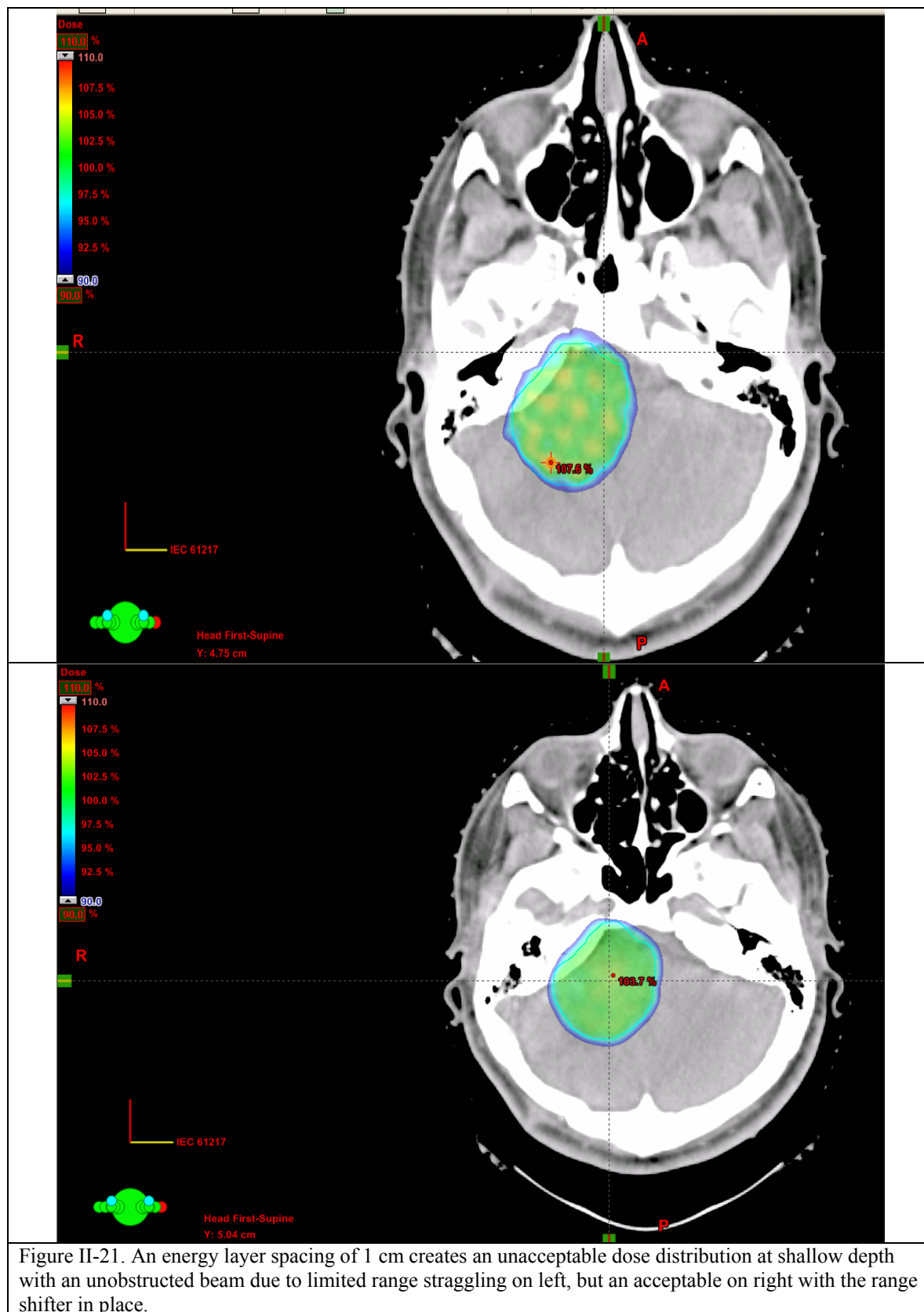
Figure II-21. An energy layer spacing of 1 cm creates an unacceptable dose distribution at shallow depth with an unobstructed beam due to limited range straggling on left, but an acceptable on right with the range shifter in place.

For next quarter, Derek will continue James' investigations in treating shallow depths. He will work towards validation of the Eclipse PCS algorithm using these devices commissioned as add-ons. He will incorporate the range shifter and ridge filter simulations into the kernel generation code, so that we can study treatment planning with these devices, and compare to Eclipse-optimized treatment plans.

III. <u>Image-Guided and Adaptive Proton Radiotherapy</u>

Protocol Development

In previous years we reported on a group of protocols that were being developed for treating different sites with proton therapy. During the past year we started submitting these protocols for DOD approval. At that point it was determined that, because the studies would not use DOD funds, they did not need DOD approval. We returned the funds used to develop these protocols and instead funded the work with department funds. There are two exceptions to the above:

1- One protocol on adaptive planning studies has been submitted for DOD approval and is now in the hands of Dr Jeffery Stephenson at TATRC. The purpose of this study is to quantify the changes that take place during radiotherapy by performing imaging studies throughout a course of treatment. For patients receiving proton therapy it is particularly important to understand changes in anatomy because those changes can affect the range of the proton beam and therefore the dose coverage.

2- The protocols developed at Penn and in which the WRAMC physicians decide that they want to enroll their DOD patients. The protocol review for these studies will go through the normal process that WRAMC uses which includes approvals at several levels. It should be noted that there is a distinction between patients referred to Penn for therapy and patients for whom the WRAMC physicians are attending for all or part of the treatment. In the first group, the patients can enroll in Penn studies whether the protocol is approved by DOD or not. This is analogous to when WRAMC patients are referred to MGH or any other center for treatment.

CBCT on the gantry

It has been a struggle to find an approach to equip the proton rooms with the ability to perform a cone-beam CT. Initially, the plan was to attach the Varian system to the IBA gantry. After the engineering studies were done, that plan proved too expensive. Next we investigated partnering with other proton centers to mount the Elekta CBCT on the ceiling of the gantry room. This got to the prototype stage and seemed promising but Elekta decided that the market for such a system was too small and they stopped development. Now, in 2010, IBA has decided to investigate using the existing imaging panels for CBCT. It is not clear that this will work but testing has begun.

Review & changes to the SOW

Because of the changes made in SOW for this award we will have an AIBS review in September. We will propose new projects and a timescale that we would like to use the funds that remain in this award. If the CBCT project does not develop, there will be over $3 million that will be unspent. We will also seek the advice from the reviewers on the best allocation of the remaining funds. It should be noted that the funds are not just from the unspent money on protocols and CBCT but also include the fact that we decided not to use a six degree-of-freedom couch top in the setup room and that the PET-CT came in significantly under budget when we decided to be a beta-site for the new Philips scanner.

IV. Report from the Walter Reed Army Medical Center group

Research in Monte Carlo Simulations and Dosimetry Studies of Proton Therapy
Rulon Mayer, PhD

Energetic protons used to damage tumors while sparing normal, healthy tissue has recently become increasingly popular among medical research institutions. The increased use of protons is attributed to the controllable and better spatial dose distribution from the "Bragg peak" for treating tumors relative to more standard radiation therapies such as electrons and x-rays. As in other types of radiations, the presence of tissue heterogeneity (or tissues that have densities departing from water such as cavities, bone etc.) within the treatment field is expected to affect the dose distribution of proton therapy. These dose distributions must be accounted for in the treatment plan in order to provide predictable, accurate and optimal therapy. This highly spatially directed therapy can potentially deliver better therapeutic doses but only if it can given predictably and can quantitatively account for any discrepancies in standard conditions.

Most studies have used Monte Carlo simulations to determine the dose perturbation due to the presence within the treatment field of tissue heterogeneities. Such an approach is flexible and can analyze a wide variety of situations. However, Monte Carlo simulations are computationally intensive and time consuming relative to those used in treatment planning. Therefore the treatment planning systems use simplified approaches for assessing tissue heterogeneities and it is affect on radiation dose delivered to tumors and vital organs. It is valuable to present experimental feedback to validate the simplified and Monte Carlo calculations. Presently, there is a dearth of direct experimental confirmation of the calculations and this research effort will attempt to reduce that deficit in knowledge.

As of April, 2010, there has been a shift in research direction away from the Monte Carlo simulations. Due to the recent change in effort, there has been limited progress due to the short time span (April 2010 to May 2010). However, this effort has developed a plan, acquired the needed supplies, and developed and tested software.
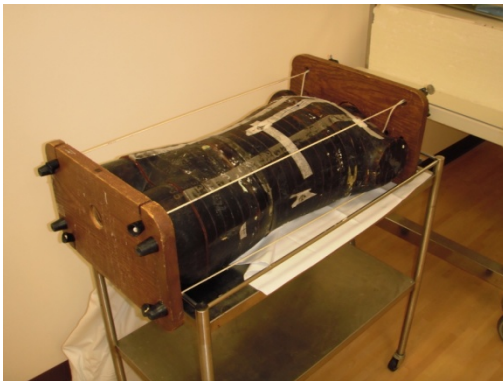

Figure 1. Human Phantoms to be used to assess radiation exposure to abdomen, thorax, and head.

Specifically, this research effort will examine and test the proton dose delivered to the head and abdomen areas that are affected by tissue heterogeneities in plastic human phantoms. Radiochromic media will be sandwiched between slabs of plastic phantom with varying density identical to the human tissues and cavities. The film-like media will be exposed to proton beam radiation under situations mimicking that expected for a typical plan for treating the abdomen, thorax and head areas. Radiochromic media, a polymer based material darkens upon exposure to radiation similar to film. However, radiochromic media has the virtue of being energy insensitive, unlike x-ray film, and therefore can be simply evaluated to determine dose distributions. The extended detection area can be evaluated to determine the dose delivered over large areas and to compute the dose-volumetric histograms for affected normal tissues. The dose-volume histogram is a standard quantitative metric for predicting clinical outcome due to radiation

exposure. The extended area dosimetry, unlike point dosimeters such as ionization chambers and thermo luminescent detectors, makes it feasible to make such computations. Selective use of point dosimeters will help confirm the extended area dosimetry.

The approach is devised to generate quick results with only small investments in money and limited personnel (one person). For example, this effort has developed in-house custom software to analyze digitized output of existing film scanners (Vidar 16) within the Walter Reed Clinic or cheap commercial document scanners (CanonScan LiDE 700F, ~$150) of standard x-ray films and radiochromic media. For example, (Figure 2a) shows depth dose captured by a film sandwiched between plastic phantom to 6 MV photons for 10 cm x 10 cm field. In house software converted the grey levels to dose (Figure 2b) with the aid of calibration films. A fictitious "proton organ" (displayed as yellow) is shown in Figure 2c and in-house software computes a dose-area histogram (Figure 2d). In contrast, conventional dosimetry film scanners and software cost ($15,000). The research plan also hopes to avoid unnecessary travel and waste in time and personnel through its development in stages.

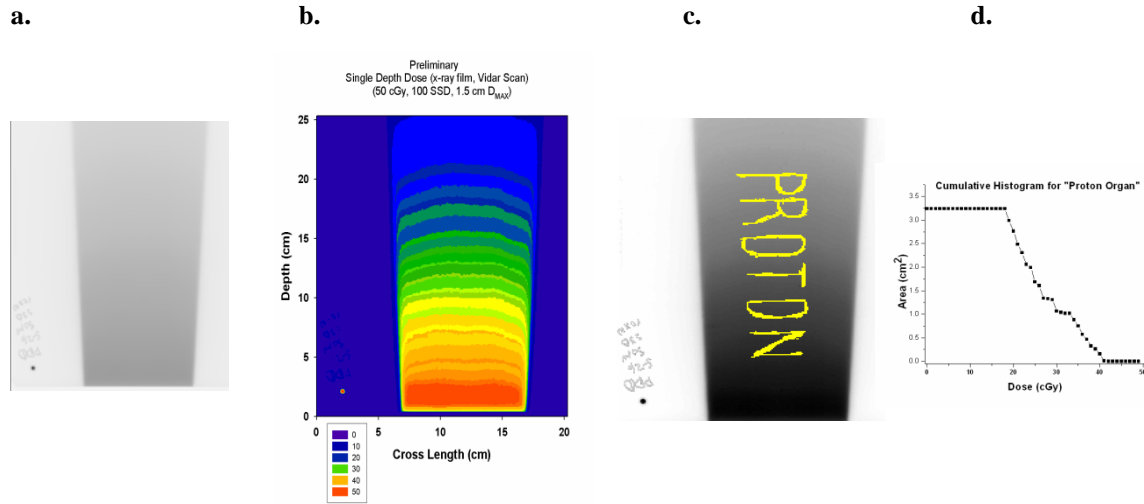**a.**   **b.**   **c.**   **d.**

Figure 2. (a) X-ray film sandwiched between water-equivalent plastic exposed 50 cGy, 100 SSD, 6 MV x-rays. X-rays enter the phantom from below and penetrate and scatter inside the plastic. (b) Grey Levels converted to dose using procedure outlined in this Review and displayed as Isodose contours.(c) "Proton" organ superimposed onto exposed film. (d) Cumulative histogram for "proton" organ

Project will proceed in three steps. First x-rays will expose film and radiochromic media to a single field and compare the dosimetry with the treatment plan (Figure 2). The purpose of this step is to perfect and refine the scanning, soft-ware development and dosimetry technique. Next, radiochromic media will be inserted between the plastic slabs in the human phantom and exposed to multiple fields in a fashion similar to those used to treat patients. The human phantom will be CT scanned to determine the tissue heterogeneity and tissue location to test the dose-volume histogram of relevant tissues. Treatment plans will be generated and compared to the dosimetry derived from radiochromic media. TLDS may be inserted into the phantom to further confirm the technique. Finally, after the dosimetry issues for x-rays have been resolved, the phantom and radiochromic media will be brought to the University of Pennsylvania Proton facility and exposed to multiple proton fields in a manner used to treat patients. The radiochromic media dosimetry resulting from proton beam exposure will be compared to treatment planning system that incorporates tissue heterogeneity.

Organ motion quantification and monitoring
Yu Chen

a). Respiratory motion and 4D proton treatment planning

We plan to implement real patient tumor contoured from static 3D CT patient data into the XCAT program for clinical applications. The XCAT images with respiratory motion will be used to develop 4D proton treatment planning strategy for breast cancer and lung cancer, and to predict real-time organ/tumor imaging aided by a motion tracking system. The proposal entitled "Development of a Computerized Human Phantom for 4D Radiation Treatment Planning" was submitted for a 2009 NIH Challenge Grant (multi-institutional efforts involved by WRAMC, Duke, UPenn researchers, medical physicists and radiation oncologists). Although this proposal was not funded this time, some reviewer's comments were quite encouraging: "Incorporation of respiratory motion into the XCAT phantom and benchmarking its accuracy and resolution (both spatial and temporal) against both RPM and a spirometer operating in 4DCT with an adequate real lung-cancer patient database, has the potential to contribute significantly to 4DCT planning, and thus make an impact on the treatment efficacy for many lung-cancer patients." "The current reviewer thinks that this work is well worth doing, and would welcome a more realistic revised proposal that would have a much greater chance of success." The chief of the medical physics research group at the National Cancer Institute, Dr. Robert Miller, has shown interest in collaborating with us on this. We plan to submit a revised proposal for other funding opportunities, such as a regular NIH R01 research grant. A proposal for a NIH R01 research grant is under discussion (multi-institutional efforts involving WRAMC, Duke, UPenn, and NCI researchers, medical physicists and radiation oncologists).

b). Intra-fraction motion

A pair of kV imagers have already been installed with the proton gantry at the Roberts Proton Therapy Center of University of Pennsylvania. We are investigating using this pair of imagers to image the radiopaque markers (such as gold markers) implanted into the targeted patient organ/tumor for verification of patient positioning.

1.   Simulation Study

As the first step, the voxelized XCAT phantom was used in GATE simulation for human organ delineation. Different materials were used for different tissues such as bones, muscles. A variety of commercially available fiducial markers, such as CIVCO carbon seeds Φ 1x3 mm, gold seeds Φ 1.2x3 mm, and IBA gold Visicoil linear markers (Φ 0.35x10 mm with a wire diameter of 0.05 mm, Φ 0.75x10 mm with wire of 0.25 mm, Φ 1.10x10 mm with wire of 0.50 mm) were simulated. Different kVp x-ray spectra were generated by the TASMIP program as shown in Figure 1.
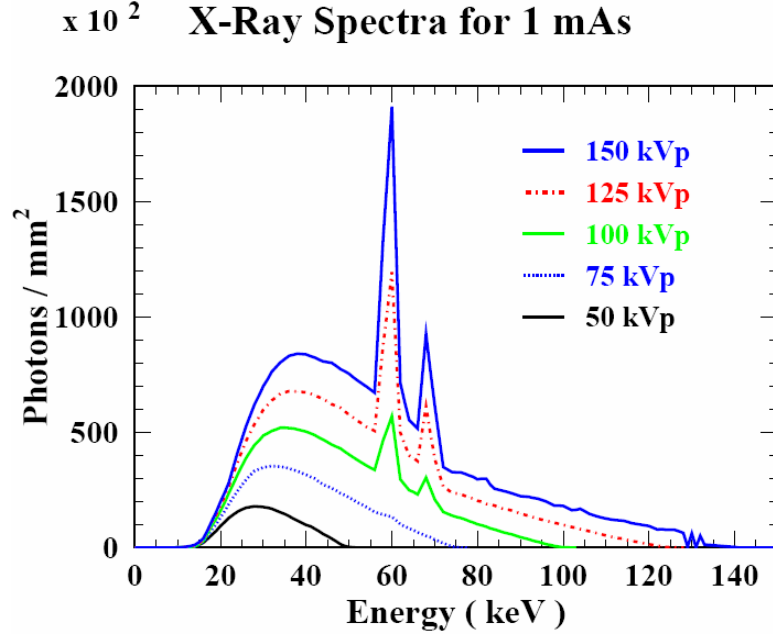
Figure 1. Normalized x-ray Spectra for 1 mAs generated by the TASMIP program for 50, 75, 100, 125, and 150 kVp.

Fiducial markers were positioned in both lateral sides (comparable to future phantom experiments). They were shadowed by the prostate and other bone or soft tissues when incident cone-beam x-rays were from the lateral direction. All penetrating photons were recorded and their energies were summed to form an image in order to compute incident contrast noise ratio (CNR) for any succeeding imager. The CNR was defined as:

$$CNR = \frac{(N_{sig} - N_{bkgd})}{\sqrt{\sigma_{sig}^2 + \sigma_{bkgd}^2}}$$

where N_{sig}, σ_{sig} are average and standard deviation for region of signal (markers) while N_{bkgd}, σ_{bkgd} are average and standard deviation for corresponding region of background (here we chose certain surrounding area of each markers). Shown in Figure 2 is the XCAT phantom projection image (2 mm pixel) from lateral direction (left) and its amplified simulated image with markers (right). The CNR was calculated for each marker and used as a quantitative measure of its visibility. Taking into account DQE etc, the observed CNRs are estimated to reduce a factor of 2. It is considered barely visible if observed CNR ~ 1. For different markers shadowed by the soft tissue and the dense bone, simulated incident CNR vs x-ray spectrum is shown in the left of Figure 3 and CNR vs x-ray fluence at 50 kVp in the right of figure 3. As shown in Figure 3, all carbon markers are invisible with CNRs under 1.0, and all gold markers shadowed by the dense bone have CNRs around 1.0. The smallest coil marker with the soft tissue has CNRs of about 2.0 for the range of 50 - 150 kVp. The Visicoil linear marker of Φ 0.75x10 mm with a wire diameter of 0.25 mm is able to produce comparable visibility as the conventional solid gold marker, with the advantages of less dense and easier volumetric localization, providing a possible measure of fast, low dose real-time target imaging.
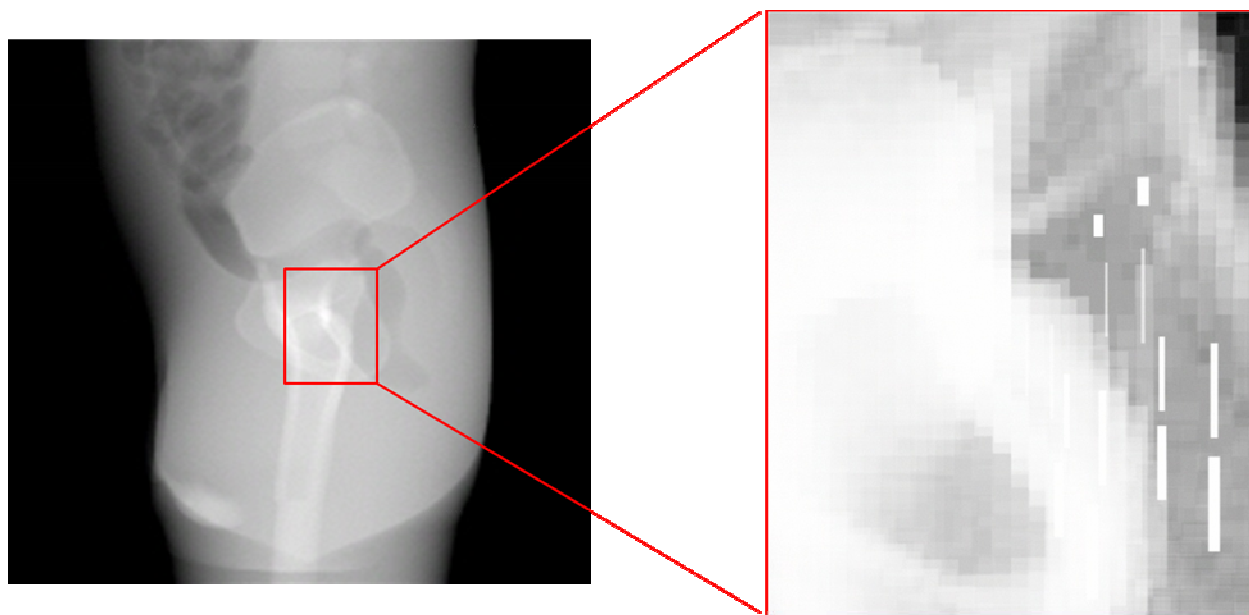
Figure 2. The XCAT phantom projection image (2 mm pixel) from lateral direction (Left) and its amplified simulated image with markers (Right).
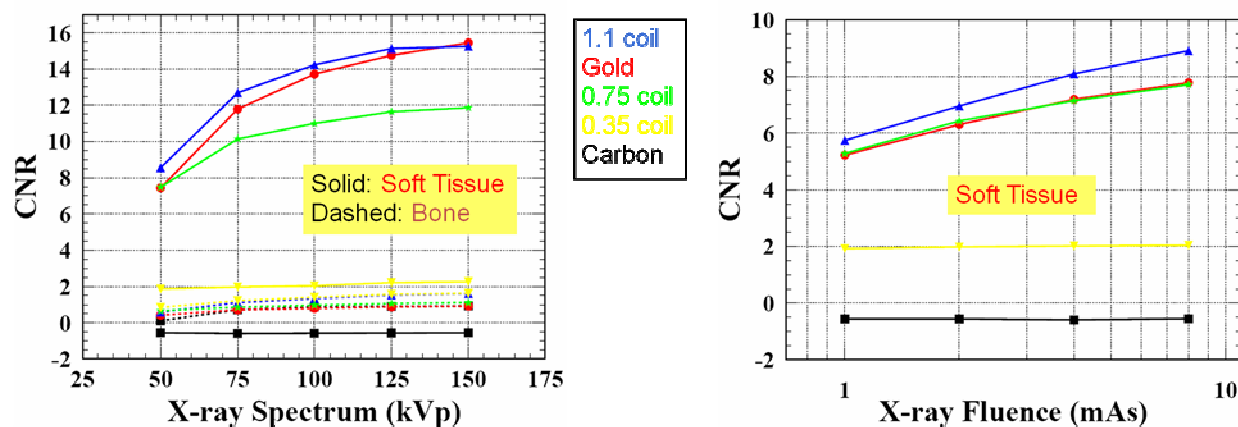

Figure 3. Simulated incident CNR vs X-ray Spectrum (Left) and Fluence at 50 kVp (Right) for different markers shadowed by soft tissue and dense bone.

An abstract of this work was submitted to PTCOG 48th annual meeting held in Heidelberg, Germany on September 28 to October 3, 2009 and has been accepted as poster presentation. The abstract is included as follows.

43

Quantitative Assessment of the Visibility of Fiducial Markers in Prostate by Monte Carlo Simulation of On-Board kV Imaging System

Yu Chen[1,2], John O'Connell[2], Christine Ko[2], and James McDonough[3]

1, Henry M. Jackson Foundation for the Advancement of Military Medicine, Rockville, MD
2, Radiation Oncology Service, Walter Reed Army Medical Center, Washington, DC
3, Department of Radiation Oncology, University of Pennsylvania Medical Center, Philadelphia, PA

Background: Accurate target positioning and motion tracking of the prostate gland is critical for precise delivery of radiation treatment for prostate cancer patients. Gold seeds have been used for successful real-time target tracking using simultaneous kV-MV imaging in radiation therapy. Implanted gold markers, however, can cause a metal effect on CT imaging and change target density, which is a crucial effect in proton therapy. We investigate possible smaller, less dense fiducial markers that can produce comparable and acceptable visibility in a kV-kV imaging system on proton gantry.

Material and Methods: The GATE (Geant4 Application for Emission Tomography and Radiotherapy) Monte Carlo simulation package was used to simulate the imaging system. Normalized x-ray spectra for a tungsten target x-ray tube were generated by the TASMIP program for different kVp. The voxelized XCAT human phantom was used for realistic human anatomy simulation. Several commercially available fiducial markers: a solid carbon marker of ϕ1x3 mm, a solid gold marker of ϕ1.0x3 mm, and Visicoil gold linear markers of ϕ0.35x10 mm with a wire diameter of 0.05 mm, ϕ0.75x10 mm (0.25 mm wire), and ϕ1.1 x10 mm (0.50 mm wire) were positioned in both lateral sides (comparable to future phantom experiments). They were shadowed by the prostate and other bone or soft tissues when incident cone-beam x-rays were from the lateral direction. A number of photons were generated corresponding to 8, 2, 1, 0.5, and 0.25 mAs for 50, 75, 100, 125, and 150 kVp spectra, respectively. All penetrating photons were recorded and their energies were summed to form an image in order to compute incident contrast noise ratio (CNR) for any succeeding imager. The CNR was calculated for each marker and used as a quantitative measure of its visibility.

Results: All carbon markers are invisible with CNRs under 1.0, and all gold markers shadowed by the dense bone have CNRs around 1.0. The smallest coil marker with the soft tissue has CNRs of about 2.0 for the range of 50-150 kVp. Its observed CNRs with a Varian PaxScan 4030E flat panel detector (DQE ~ 30%, MTF ~ 45%) are estimated to drop to ~ 1.0, which may be considered barely visible. The medium coil marker with the soft tissue has produced CNRs of 7.5, 10.1, 11.0, 11.6, and 11.9 for 50, 75, 100, 125, and 150 kVp, comparing to those of the solid marker of 7.4, 11.8, 13.7, 14.8, and 15.5. For 1, 2, 4, and 8 mAs under 50 kVp, CNRs are 5.1, 6.2, 6.9, and 7.5 for the medium coil marker and 2.6, 4.8, 6.4, and 7.4 for the solid marker.

Conclusion: The carbon marker is not suitable for the purpose of real-time kV target imaging. Other markers are difficult to see if they are shadowed by dense bone. The long linear coil marker may be easier to extend beyond the dense bone region. The Visicoil linear marker of ϕ0.75x10 mm with a wire diameter of 0.25 mm is able to produce comparable visibility as the conventional solid gold marker, with the advantages of imaging under low energy and low fluence, providing a possible measure of fast, low dose real-time target imaging.

2. Experimental Study

The experiments using a pelvic physical phantom and real markers were conducted in the proton gantry room on September 17 and 18, 2009 for imagine through lateral direction. A variety of commercially available fiducial markers, CIVCO carbon seeds Φ 1x3 mm, gold seeds Φ 0.8x3 mm and Φ 1.2x3 mm, and IBA gold Visicoil linear markers (Φ 0.35x5, x10 mm with a wire diameter of 0.05 mm, Φ 0.50x5, x10 mm with wire of 0.15 mm, Φ 0.75x5, x10 mm with wire of 0.25 mm, Φ 1.10x4, x10 mm with wire of 0.50 mm) were investigated in this experiment. The

experimental setup is shown in Figure 4. In this system, the flat panel detector is a Varian PaxScan 4030E (DQE ~ 30%, MTF ~ 45%) and the x-ray tube is a Varian A-277 with an output range of 50 – 150 kVp.
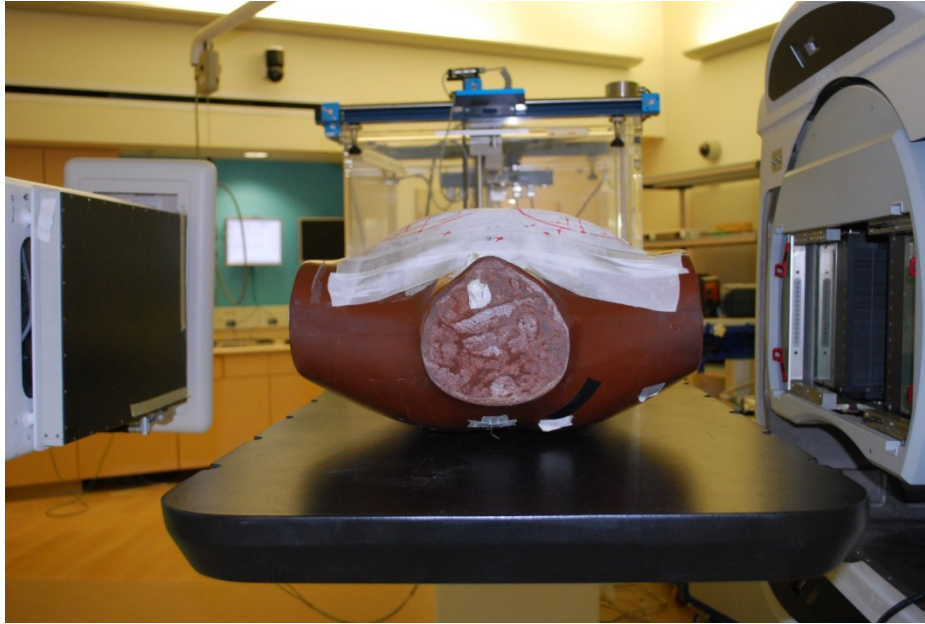

Figure 4. Experimental setup. A whole body phantom is positioned between a x-ray tube (inside of the proton beam nozzle in the right) and a flat panel detector in the left.

Fiducial markers were positioned in both lateral sides of the pelvic phantom. They were shadowed by the bone or soft tissues when incident cone-beam x-rays were from the lateral direction. A typical image acquired at 125 kVp, 200 mAs for the larger gold seed is shown in Figure 5.
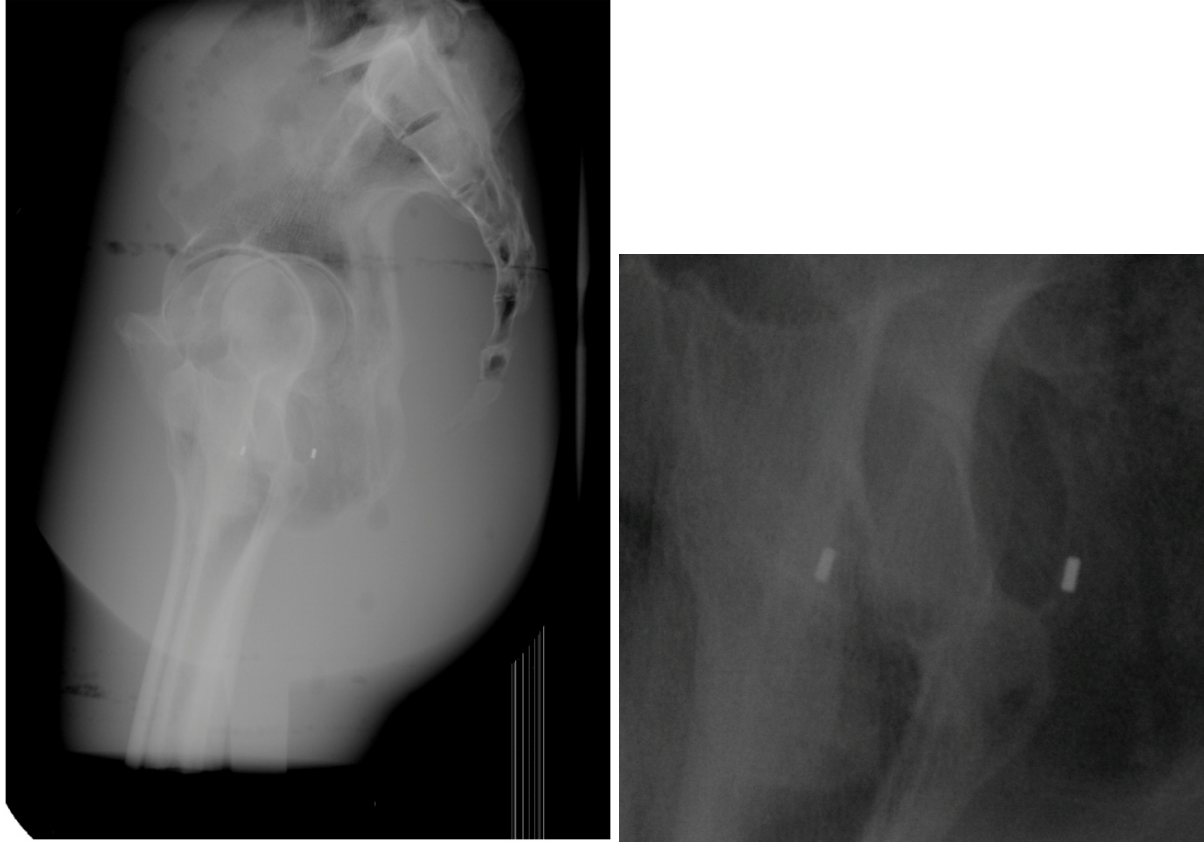
Figure 5. A typical x-ray projection image for the gold seeds 1.2x3 mm in the bone and soft tissues.

The regions of interest (ROIs) are chosen to form the marker signal and its corresponding background. The contrast noise ratio (CNR) for a given marker is calculated using the mean and standard deviation from the ROIs. For different markers shadowed by the soft tissue and the dense bone, CNR vs mAs for 125 kVp is shown in Figure 6 (the left for soft tissue and the right for the dense bone). As shown in Figure 3, if CNR > 2 is required for a better visibility, the carbon marker and the Visicoil Φ 0.35 mm marker are not suitable for the imaging of regions shadowed by dense bone.
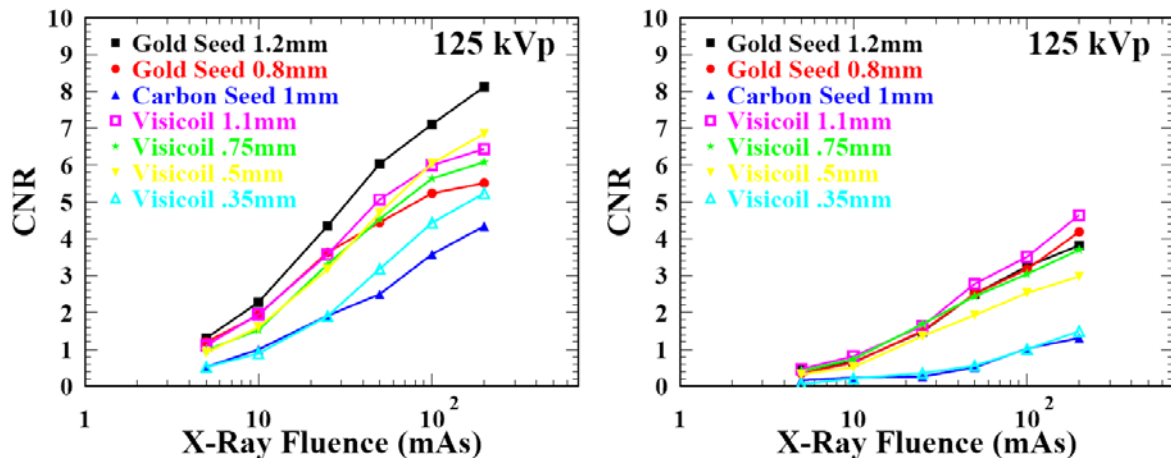
Figure 6. Measured CNR vs X-ray Fluence (mAs) at 125 kVp for different markers shadowed by soft tissue (Left) and dense bone(Right).

Typical images acquired at (125 kVp, 200 mAs) from the lateral imaging system for the two medium-sized Visicoil markers are shown in Figure 7. The image quality can be characterized by the signal noise ratio (SNR), which can be calculated by dividing mean by standard deviation for a given region of interest (ROI). Acceptable image quality requires SNR > 20. From Figure 8, it is observed that the image quality for the bone region would be good for > 50 mAs at 75 kVp or > 10 mAs at 100 kVp.
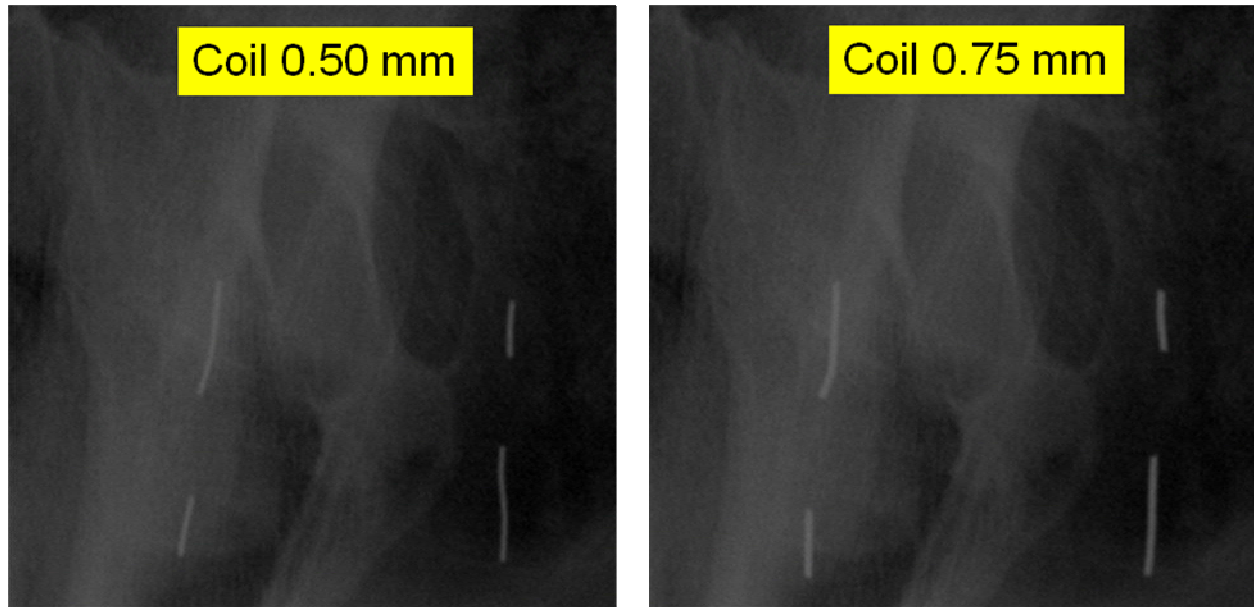

Figure 7. The projection images at (125 kVp, 200 mAs) for the linear markers of Φ 0.50 x5 mm, x10 mm (Left) and Φ 0.75 x5 mm, x10 mm (Right) in the regions through the dense bone and soft tissues through the lateral direction.
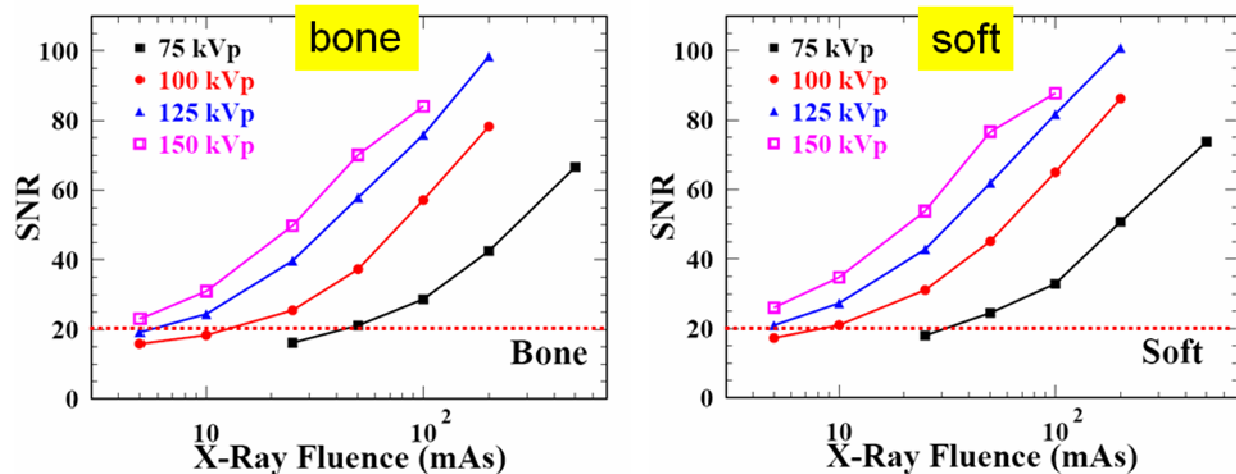
Figure 8. Measured SNR vs X-ray Fluence (mAs) at various kVp for the regions through the dense bone (Left) and soft tissues (Right).

To optimize the system setting, a series of measurements have been done for each marker in the range of 75 - 150 kVp and 5 – 500 mAs. Shown in Figure 9 are CNRs in the bone region for the Visicoil linear markers of Φ 0.50x5 mm and Φ 0.75x5 mm. For an acceptable visibility of markers of CNR > 2, it requires that > 140 mAs at 100 kVp

or > 50 mAs at 125 kVp for the Φ 0.50x5 mm marker and that > 100 mAs at 100 kVp or > 30 mAs at 125 kVp for the Φ 0.75x5 mm marker. Currently the Roberts Proton Therapy Center uses the Visicoil Φ 0.50x5 mm marker implanted in patient's prostate for lateral imaging at (100 kVp, 200 mAs).
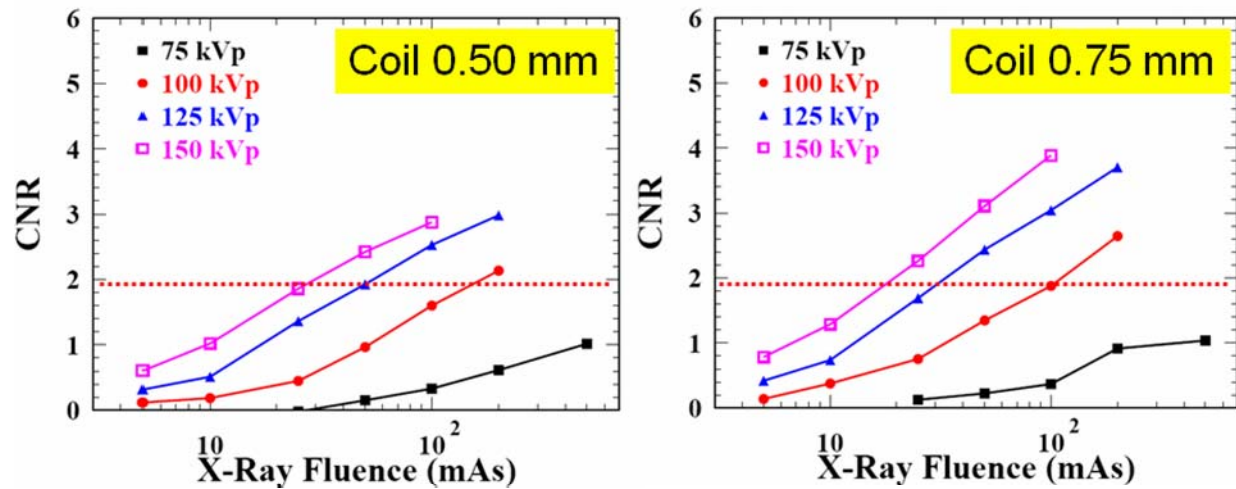
Figure 9. Measured CNR vs X-ray Fluence (mAs) at 75, 100, 125 and 150 kVp for the linear markers of Φ 0.50x5 mm (Left) and Φ 0.75x5 mm (Right) in the region through the dense bone.

Furthermore, we compared relatively the x-ray exposure doses in different conditions. A dose monitoring system hung on the proton gantry room as shown in the left of Figure 10 and was used to record doses in the room. Normalized doses were plotted in the right of Figure 10. It is observed that while (100 kVp, 200 mAs) and (125 kVp, 100 mAs) can give comparable image quality and marker visibility the dose at (125 kVp, 100 mAs) is less than that at (100 kVp, 200 mAs). An abstract of this work was submitted and accepted for a poster presentation to PTCOG 49th annual meeting held in Japan in May 20-22, 2010.

Figure 10. The dose monitoring system (Left) and normalized doses under different conditions (Right).

48

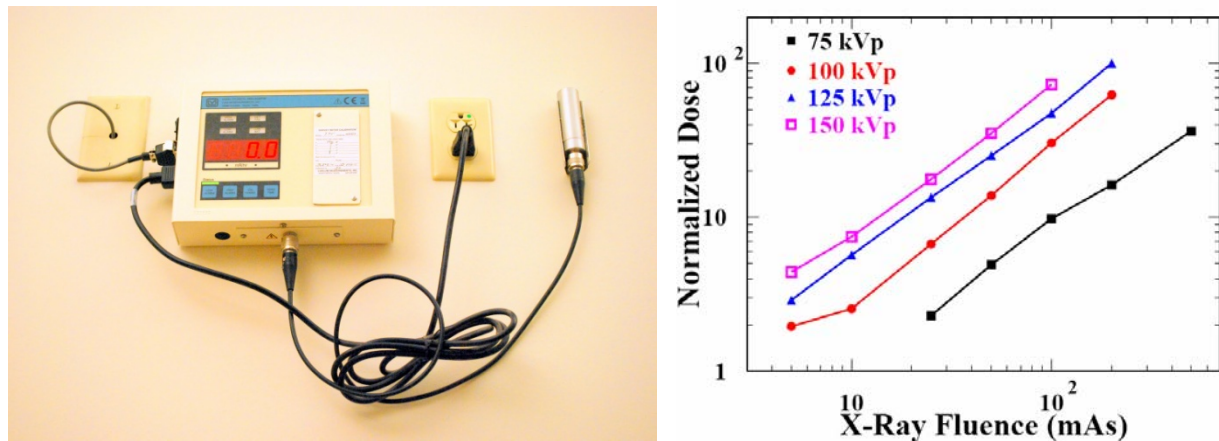Experimental Study on the Visibility of Fiducial Markers and Optimal Settings for On-Board kV Imaging System at Proton Gantry

Yu Chen[1,2], John O'Connell[2], Christine Ko[2], and James McDonough[3]

1, Henry M. Jackson Foundation for the Advancement of Military Medicine, Rockville, MD
2, Radiation Oncology Service, Walter Reed Army Medical Center, Washington, DC
3, Department of Radiation Oncology, University of Pennsylvania Medical Center, Philadelphia, PA

Purpose: To investigate possible smaller, less dense fiducial markers implanted into the patient's targeted organ/tumor for the verification of patient positioning that may produce comparable and acceptable visibility regarding to conventional gold seeds in a kV-kV imaging system on the proton gantry at the Roberts Proton Therapy Center of University of Pennsylvania.

Methods: The experiments used a pelvic phantom and real fiducial markers: VISCON carbon seeds 1x3 mm, gold seeds 0.8x3 mm and 1.2x3 mm, and IBA gold Visicoil linear markers (0.35x5, x10 mm with a wire diameter of 0.05 mm, 0.50x5, x10 mm with wire of 0.15 mm, 0.75x5, x10 mm with wire of 0.25 mm, 1.10x4, x10 mm with wire of 0.50 mm). The fiducial markers were positioned on the lateral sides of the pelvic phantom. The kV imaging system consists of a flat panel detector (Varian PaxScan 4030E) and an x-ray tube (Varian A-277). To optimize the system setting, measurements were made for each marker in the range of 75 - 150 kVp and 5 – 500 mAs. The contrast noise ratio (CNR) for a given marker was calculated and used as a quantitative measure of its visibility.

Results: No significant improvement is observed by increasing the length of the linear markers from 5 mm to 10 mm. If CNR > 2 is required for acceptable visibility, the carbon marker and the smallest Visicoil marker are not suitable for the imaging through dense bone. The linear coil markers of 0.50x5 mm and 0.75x5 mm are most suitable for the projection imaging through both the soft tissue and dense bone, and are able to produce comparable visibility as the conventional solid gold markers.

Conclusions: The medium sized 0.50-0.75 mm coil markers may provide a possible measure of fast, low dose real-time target imaging with the advantages of lower density and easier volumetric localization. In terms of the visibility of markers, patient image quality, and exposure dose, an optimal range of 120-130 kVp and 50-100 mAs is suggested for imaging these markers in a patient's body.

This work was supported by the US Army Medical Research and Materiel Command under Contract Agreement No. DAMD17-W81XWH-04-2-0022. The views, opinions, interpretations, conclusions and recommendations expressed in this abstract are the authors and do not reflect the official policy of the Department of Army, Navy, Department of Defense, or US government.

On March 18-19 and May 13 of 2010, we conducted experiments for those markers imaged through the posterior-anterior direction (vertical to the proton beam direction) using the AP x-ray imager system. The data for P-A direction is to be analyzed. The experimental setup is shown in Figure 11. Both orthogonally positioned imaging systems consist of a flat panel detector (Varian PaxScan 4030E) and a x-ray tube (Varian A-277). After all data analysis has been done, we plan to submit these results to the journal of Medical Physics for publication.

Figure 21. Experimental setup. A whole body phantom is positioned on a patient table with one system imaging through the lateral direction and another through the posterior-anterior direction.

c). On-line positron emission monitoring in proton therapy

It is demonstrated by some investigators that on-line and/or shortly after treatment PET scans can be valuable for dose delivery verification. The research teams at WRAMC and UPenn have extensive experience on Monte Carlo simulation using Geant4. An international OpenGATE Collaboration is extending their efforts from simulating Emission Tomography (PET and SPECT) to radiotherapy by developing GATE (Geant4 Application for Emission Tomography and Radiotherapy). We applied the GATE Collaboration membership and have been officially approved as two separate member groups of HJF/WRAMC and UPenn. Dr. Yu Chen and Dr. Stephen Avery are contact persons for HJF/WRAMC and UPenn groups, respectively. By joining the GATE Collaboration, we committed to implement our simulation software into the GATE framework and meanwhile share other member's results of voxelized dosimetry calculation. Drs. Chen participated in the GATE Workshop held as part of the IEEE Nuclear Science Symposium and Medical Imaging Conference in Orlando, Florida October 25 – 31 to meet the GATE members for discussions of our research plans.

As two institutional members of the international OpenGATE Collaboration among other four US members, we started to verify GATE V6 (Geant4 Application for Emission Tomography and Radiotherapy) which was publicly released on February of 2010. We first found a bug in the software by running it in Mac X OS system. A new patch

50

to fix this and other bugs was then released on May of 2010. We will start to use GATE to simulate the UPenn partial ring PET prototype and the Philips Gemini TF PET/CT scanner already in the Roberts Proton Therapy Center once the GATE software can be successfully run in our Mac cluster.

We spoke to Dr. Ling Shao, Director of Imaging Physics and System Analysis Nuclear Medicine of Philips Healthcare, to seek help on simulating Philips Gemini TF PET/CT scanner already in the Roberts Proton Therapy Center. Our long term goal is to simulate and measure proton-induced positron isotope distributions at different time periods after proton beam treatment taking into account the organ/tumor motion.

Remote Proton Radiation Therapy (RPRT) telemedicine solution
Arnaud Belard

a) Tandberg videoconferencing unit

During this period, four additional Tandberg units were acquired and deployed to locations likely to be involved in remote proton radiation therapy planning: NNMC (two units), WRAMC (three units), MAMC (one unit), BAMC (one unit). This brings the total number of videoconferencing units to eleven (including one deployed at UPenn).

b). Connectivity to the University of Pennsylvania

Full bilateral connectivity remains elusive. Initial problems were attributed to a configuration setting with the long-distance carrier UPenn uses for outbound/inbound ISDN calls. Once resolved, another issue was identified, one which prevents UPenn from receiving video signal from Walter Reed.

Multiple tests were conducted this past year, involving not only Walter Reed and UPenn, but also Polycom, RoData (provider of the RMX2000 videoconferencing bridge), Criticom (provider of the Tanderbg 1700 MXP desktop VTC units), and USAMITC engineers. We were initially told by RoData-Polycom to capture logs of calls placed by both institutions, which were provided over the course of several weeks (i.e. multiple tests, which involved both 'pass' and 'fail' calls). We were subsequently asked to disable some of the features of the units to identify which of the protocols was/were causing the video transmission issue.

H.239 (content-sharing) and H.264 / H.263 (transmission protocol for audio-video transmission) were disabled sequentially. We did achieve complete connectivity using the much older H.261 protocol, but the video-quality was sub-optimal.

To eliminate yet another potential cause, both Walter Reed and UPenn upgraded their Tandberg 1700 MXPs and RMX2000 MCU to the latest software version (respectively 8.2 and 2.0). Subsequent tests showed that the upgrade had no meaningful impact on connectivity (i.e., the majority of calls still failed to produce incoming video for UPenn).

The latest test, this time involving engineers from the USAMITC bridge, yielded a possible cause. According to the release notes for the CODIAN gateway 2.0, bug ID 2867 could explain our inability to have full connectivity. During this latest series of tests, logs were captured and subsequently sent to the Tandberg development team (escalated to Tier 3 at Polycom as well). The 'bug ID 2867' entry is being inserted here for reference.

This bug applies to calls from an IP endpoint (1) -> an MGC gateway -> Codian ISDN GW -> IP endpoint (2). This bug causes IP endpoint (2) to not receive any video. There is a workaround for this situation: use the MGC as an MCU instead of as a gateway. That is, make a direct ISDN call from an MGC conference to IP endpoint (2) through the Codian ISDN GW and the call will be fully connected. Then from the same conference, call the IP endpoint (1) over H.323. For this workaround to work, the 'Transcoding' option on the MGC conference must be enabled. As there are only two endpoints in the conference, the call will appear to the callers in the same way as a point-to-point call over an MGC gateway.

The latest update from Tandberg indicates that the development team was able to replicate the issue in their own lab and are working with Polycom to address the problem. It is likely this bug will be resolved in a forthcoming software patch. Until then, since no workaround currently exists, may have to use the older H.261 protocol to conduct our on-going tests.

RPRT – CITRIX / TANDBERG solution (VTC)
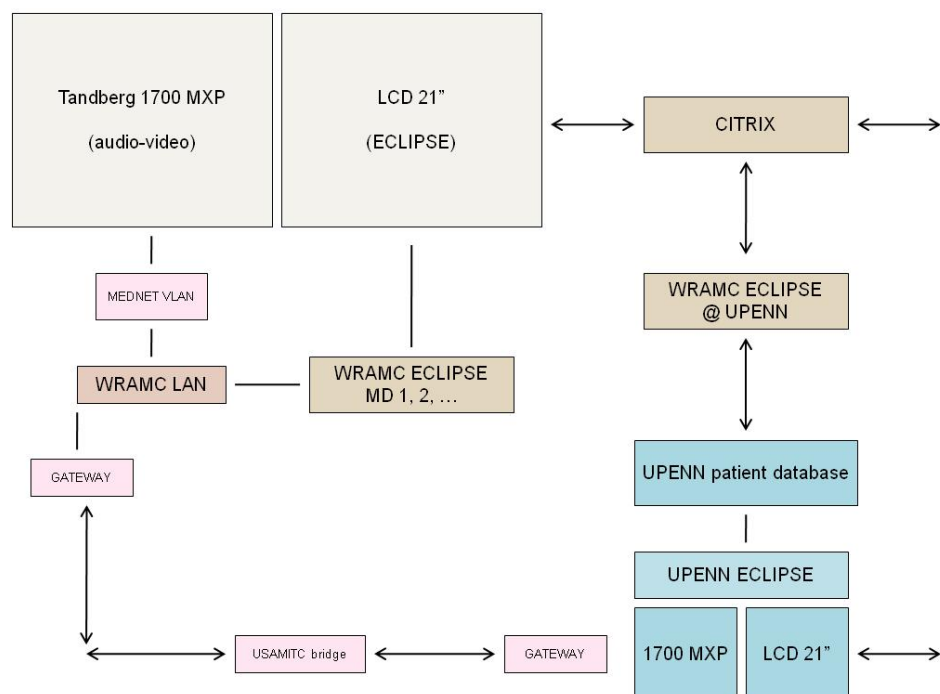
c). Application-sharing: Polycom PVX to Adobe Connect to CITRIX

Over the life of this grant, the search for a robust application-sharing tool has presented us with several challenges. Initially encouraged by the Directorate of Information Management (WRAMC-DOIM) to use Polycom PVX as a simple-to-use and cost-effective platform for the sharing of remote applications, we were then steered towards Defense Connect Online (DCO), a DoD-managed version of the popular Adobe Connect application,

Along the course of evaluating this package, we were told by DCO that due to sessions being recorded and stored (with data potentially accessed by non-HIPAA certified staff), the use of this platform as a virtual medical simulation tool would have to be suspended until the HIPAA issue could be addressed appropriately. Numerous exchanges took place between our group and DCO as we constantly engaged them on the possibility of using this particular platform for data-collaboration (other military treatment facilities have expressed interest in using this web-collaboration tool for clinical use so there seems to be MEDCOM-wide interest). The benefits of this existing solution were many (free, flexible, DOD-managed/sponsored, meets our 'application-sharing' requirements) and we felt confident we could make a case to either 1) have monitors receive HIPAA training or 2) receive an outright exemption from monitoring. Unfortunately, our efforts yielded little traction and we were thus forced to look to another alternative, one which would not only meet the security requirements of the DoD but also be HIPAA-certified.

Following a demonstration by Varian Medical Systems (provider of the Eclipse treatment planning package used for both conventional and proton radiation therapy), our program settled on the CITRIX solution to power the application-sharing portion of our telemedicine solution:

. Ability to securely transfer CT sets from the local workstation (where the CITRIX client is activated, i.e. at WRAMC) to the remote workstation (where the patient plan will be generated and stored, i.e. at Penn);

. Ability to connect to the Penn workstation to engage in the remote treatment planning of DOD patients, as stated in the grant's research goals;

. Ability to application-share with the remote site (resolving, in an ad-hoc manner, planning and/or setup discrepancies).

The system was purchased in the first quarter of 2010 and subsequently delivered/installed at the UPHS Data Center in Newark in May. Configuration will take place once we have determined whether the server will point to an existing Eclipse calculation engine (provided by the DoD to Penn, pending legal review) or a new one (to be purchased by the University of Pennsylvania, for dedicated use by the DoD). Once the CITRIX server has been configured, we expect to test the system thoroughly (simulated cases, using dummy treatment plans) before it can be used 'operationally' by the end of this year.

RPRT - CITRIX solution (remote treatment planning)
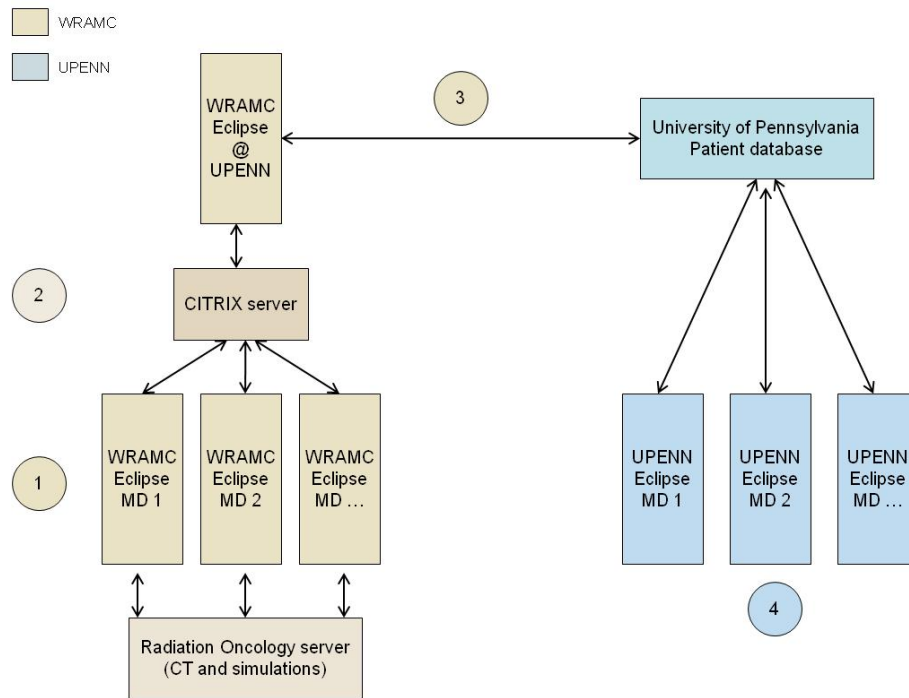
1 . Virtual tumor board (via VTC ; see next slide) with Penn confirms DOD patient eligibility for treatment
. Patient is entered into the system ; CT scans and simulations are performed in anticipation

2 . Physician uses CITRIX client to connect to DOD Eclipse workstation at UPENN
. Physician exports CT scans to remotely plan the treatment

3 . Treatment plan is saved onto UPENN's patient database

4 . UPENN physician imports treatment plan into his UPENN Eclipse workstation
. UPENN physician re-runs the calculation and validates the plan for delivery
(possible use of VTC w/ data collaboration between institutions, should issues arise)

d) Date User Agreement and New System Questionnaire forms

Since the summer of 2009, our program worked tirelessly to get a Data User Agreement signed between the Walter Reed Army Medical Center and the University of Pennsylvania. This document, which formalizes the use of the telemedicine solution and its underlying patient data, went through several versions (and subsequent legal reviews). A final document was signed in May 2010 (please see attached), along with a System Assurance Questionnaire.

Administrative Update
Arnaud Belard

1. Personnel

After three years on the program, Kevin Kramer (PhD) resigned during the first quarter of 2010 to pursue other opportunities in the field of computational physics. Rulon Mayer (PhD) was subsequently hired to fill the position left vacant. Dr. Mayer has considerable experience extending from medical physics to image-processing. Ms. Kathleen Noel and Ms. Jean Petrov, both research nurses, were also added to the research program as assistant-investigators.

As stated in our previous reports, although our team of co-investigators consists of over 30 individuals, the vast majority is federally-employed and is therefore not deriving any salary from the grant (i.e. only the three full-time Henry M. Jackson Foundation employees are compensated via this funding stream).

2. Budget

The personnel "surplus" highlighted in previous progress reports has translated into a no-cost extension of this particular phase of research, now ending mid-June 2010 (the initial end-date was May 2009). The thirteen-month delay results primarily from the accumulation of unspent salaries for the vacant research scientist positions (gap between a resignation and a new hire or abnormal delay in finding a suitable profile for a new position).

Because the delay in spending our funds is so great (thirteen months), it is likely that no-cost extensions will be requested for subsequent phases of research.

3. Publications

The article entitled 'Development of a Remote Proton Radiation Therapy Solution over Internet2' was published in the Journal of Telemedicine and e-Health (December 2009 issue). A second article, entitled 'A Hybrid Integrated Services Digital Network–Internet Protocol Solution for Resident Education', was published in the May 2010 issue of the same Journal.

The study entitled 'Comparison of Dose Volume Distributions between Protons and Conventional Photon Irradiation in the Treatment of Stage I Seminoma with Predictions of Second Malignancy Rates' conducted last year yielded a manuscript which is currently being reviewed by the International Journal of Radiation Oncology.

4. Abstracts and presentations

2009 Particle Therapy Co-Operative Group annual conference (Heidelberg, Germany):

. Dosimetric comparison of parallel opposed-laterals versus parallel opposed-laterals plus an anterior field for proton therapy prostate

. Comparison of dose volume histograms of normal structures between proton and conventional photon irradiation with adaptive radiotherapy in stave IV head and neck cancer

. Comparison of predicted excess secondary malignancies and normal tissue toxicities between proton and photon irradiation in the treatment of stage I

. Quantitative assessment of the visibility of fiducial markers in prostate by monte-carlo simulation of on-board KV imaging system

. Improving proton therapy accessibility through seamless electronic integration of remote treatment planning sites

. Ability to use telemedicine platforms to teach proton treatment planning at multiple locations as demonstrated in resident education

2010 Particle Therapy Co-Operative Group annual conference (Chiba, Japan):

. Quantitative Assessment of the Visibility of Fiducial Markers in Prostate by Monte Carlo Simulation of On-Board kV Imaging System

2010 American Society for Radiation Oncology annual conference (San Diego):

. Electronic Integration of Radiation Oncology Clinics via Remote Proton Radiotherapy Telemedicine Solution

Key Research Accomplishments

The major accomplishment of the past year has been the successful clinical implementation of the multileaf collimator in the Roberts Proton Therapy Center.

Reportable Outcomes

The following abstracts based on work performed on this project have been accepted during the past year at scientific meetings:

1. Comparison of Proton MLC with Non-Divergent Brass and Tungsten Apertures; M Kirk, C Ainsley, J McDonough; 2010 American Association of Physicists in Medicine meeting; Philadelphia PA.

2. Treatment Time Reduction for Proton Modulated Scanning Beams Using a Ridge Filter; J Durgin, D Dolney, J McDonough; 2009 American Association of Physicists in Medicine meeting; Philadelphia PA.

3. Experimental Study on the Visibility of Fiducial Markers and Optimal Settings for On-Board kV Imaging System at Proton Gantry; Yu Chen, John O'Connell, Christine Ko, and James McDonough; 2010 PTCOG meeting; Gunma, Japan.

Conclusions

This report documents the work that has been accomplished during the sixth year of the project to design an MLC for proton radiotherapy, the fifth year of work on the scanned beam project, and the fourth year of work on the image-guided proton therapy project. It concentrates on the past quarter since reports on the other quarters already have detailed those efforts. Together with our colleagues at WRAMC we continue to develop the telemedicine component including remotely operating the treatment planning system. In January 2010 we started patient treatments using the MLC.

Appendix I

Quarterly Report

1. Award No. W81XWH-04-2-0022 (Penn Fund # 542520)

2. Report Date: 15 June 2010

3. Reporting period: April 1, 2010 – May 31, 2010

4. Principal Investigator: James E. McDonough

5. Telephone No.: 215-615-5632

6. Award Organization: University of Pennsylvania

7. Project Title: "Development of a Multileaf Collimator for Proton Radiotherapy"

8. Current staff, role and percent effort of each on project.

STAFF MEMBER	ROLE	% EFFORT
James McDonough	PI	25
Steven Avery	Co-Investigator	40
Samuel Dilanni	Grants Administrator	10
Richard Maughan	Co-Investigator	15
James Metz	Co-Investigator	10
Rosemarie Mick	Statistician	15
Zelig Tochner	Co-Investigator	15
Derek Dolney	Postdoc Researcher	100
James Durgin	Graduate Student	100
Maura Kirk	Graduate Student	100
Ramesh Rengan	Co-Investigator	30
Susan Prendergast	Research Nurse	5
Tiffany Sharkoski	Clinical Research Coordinator	10

9. Contract expenditures to date (as applicable):

COST ELEMENTS	THIS QUARTER	CUMULATIVE
Personnel	$ 71,253.31	$ 2,438,999.56
Fringe Benefits	16,681.16	608,869.36
Supplies	611.70	81,195.87
Equipment	-	5,107,270.92
Travel	-	42,499.48
Other Direct Costs	253,079.22	2,148,569.54
Subtotal	341,625.39	10,427,404.73
Indirect Costs	52,352.28	1,922,443.81
Fee		
Total	$ 393,977.67	$ 12,349,848.54